Ultrafast photochromism in metal-organic complexes

by

Paul-Franzl Xavier von Stein

Thesis presented in partial fulfilment of the requirements for the degree of Master of Science in Laser Physics in the Department of Physics at Stellenbosch University

Department of Physics,
University of Stellenbosch,
Private Bag X1, Matieland 7602, South Africa.

Supervisors:

Prof Heinrich Schwoerer

Dr Gurthwin W. Bosman

Dr Christine M. Steenkamp

December 2016

Stellenbosch University https://scholar.sun.ac.za

Declaration

By submitting this thesis electronically, I declare that the entirety of the work contained therein is my own, original work, that I am the sole author thereof (save to the extent explicitly otherwise stated), that reproduction and publication thereof by Stellenbosch University will not infringe any third party rights and that I have not previously in its entirety or in part submitted it for obtaining any qualification.

Date: ....December 2016 ....

Copyright © 2016 Stellenbosch University
All rights reserved.

Stellenbosch University https://scholar.sun.ac.za

Abstract

Ultrafast photochromism in metal-organic complexes

Paul-Franzl Xavier von Stein
Department of Physics,
University of Stellenbosch,
Private Bag X1, Matieland 7602, South Africa.

Thesis: MSc

December 2016

Dithizone (H_2Dz), an analytical reagent typically used in colourimetric analysis, reacts with various transition metals to form metal dithizonate complexes. These complexes display strong absorption in the visible region of the spectrum and exhibit photochromism: a photo-induced reversible transformation of the reactant to a product form with a distinctly different absorption spectrum. The photo-isomerisation of a C=N bond in the dithizone's backbone is responsible for this behaviour. This mechanism was confirmed in 2011 by the first ultra-fast study on dithizonatophenylmercury(II) (DPM), a single-liganded complex. To compliment this study, transient absorption spectroscopy was used to capture temporally and spectrally resolved spectra of the photo-induced reaction in the dithizone ligand and select two-liganded dithizontates following excitation at their absorption maxima. The ligand, as well as the two-liganded $Hg(HDz)_2$, $Pb(HDz)_2$ and $Zn(HDz)_2$ complexes showed two reaction paths following photo-excitation. The first path is associated with an evolution along the rotational isomerisation coordinate which leads to product formation and ground state recovery with a time constant of $\approx$1 ps. This is in accordance to what was found for DPM. The second reaction path leads to a re-population of the ground state with a time constant of $\approx$10 ps. A physical process could not definitively be assigned to the second pathway, although it is speculated that it may be due to an unstable intermediate along the C=N inversion coordinate. As the 1 and 10 ps paths were found to be intrinsic to the ligand, it was concluded that the second ligand does not participate in the dynamics, at least not on times below 500 ps. The $Ni(HDz)_2$ complex was not analysed in detail due to complexities that arise given the possibility of ligand-ligand interactions and possible metal to ligand or ligand to metal charge transfer processes.

Stellenbosch University https://scholar.sun.ac.za

Uittreksel

Ultravinnige fotochromisme in metaal-organiese molekulêre komplekse

("Ultrafast photochromism in metal-organic complexes")

Paul-Franzl Xavier von Stein
Departement van Fisika,
Universiteit van Stellenbosch,
Privaatsak X1, Matieland 7602, Suid Afrika.

Tesis: MSc
Desember 2016

Ditisoon (H_2Dz), 'n reagens wat tipies gebruik word in analitiese chemie, reageer met verskeie oorgangsmetale om metaal-ditisoon komplekse te vorm. Hierdie komplekse vertoon sterk absorpsie in die sigbare gebied van die spektrum en ondergaan 'n fotochromiese reaksie: 'n foto-geïnduseerde omkeerbare transformasie van die reaktant na 'n produk vorm met 'n unieke absorpsiespektrum. Die fotoisomerisasie van 'n C=N verbinding in die ruggraat van die ditisoon is verantwoordelik vir hierdie gedrag. In 2011 is hierdie meganisme bevestig deur die eerste ultravinnige studie op ditisoonfenielkwik (II) (DPM), 'n enkel-ligand kompleks. Om hierdie studie te komplimenteer, is ultravinnige absorbsie spektroskopie gebruik om tydafhanklike spektra van die fotoreaksie in die ditisoon ligand en twee-ligand ditisoon komplekse waar te neem. Die ligand, sowel as $Hg(HDz)_2$, $Zn(HDz)_2$ en $Pb(HDz)_2$ komplekse het twee reaksie paaie gevolg na foto-opwekking. Die eerste pad word geassosieer met rotasionele isomerisasie wat lei tot die vorming van die produk en herbevolking van die grondtoestand met 'n tydkonstante van $\approx$1 ps. Dit is in ooreenstemming met wat gevind is vir DPM. Die tweede reaksiepad lei na 'n herbevolking van die grondtoestand met 'n tydkonstante van $\approx$10 ps. 'n Fisiese proses kan nie met sekerheid aan die tweede reaksiepad toegeskryf word nie, hoewel daar gespekuleer word dat dit moontlik te wyte kan wees aan 'n onstabiele intermediêre toestand in die isomerisasie proses deur middel van C=N inversie. Omdat die 1 ps en 10 ps paaie intrinsieke eienskappe is van die ligand, is die gevolgtrekking gemaak dat die tweede ligand nie deelneem aan die dinamika nie. Die $Ni(HDz)_2$ kompleks is nie in diepte geanaliseer nie, as gevolg van die kompleksiteit wat veroorsaak word deur die moontlikheid van ligand-ligand interaksies en ladingsoordragprosesse tussen die metaal en die ligand.

Stellenbosch University https://scholar.sun.ac.za

Acknowledgements

I would like to thank Prof Heinrich Schwoerer, Dr Gurthwin Bosman and Dr Christine Steenkamp for their supervision and continuous support throughout the duration of this project. Thank you also to our collaborators, Prof Karel von Eschwege and Prof Jeanet Conradie, for their insightful discussions and providing the samples used in this study.

I would also like to thank Iulia Abernethy and Esraa Ahmed for their extensive assistance in the laboratory, as well as Mr T. Botha, Mr J. Germishuizen, Mr G. Louwrens and Mr E. Shields for helping with various technicalities. In particular, I would like to thank Mr P. Cornelissen and Mr T. Stehmann for assisting with LabView related queries. To my family, friends, and particularly Michelle Jooste, thank you for your support during the last two years. Finally, I would like to thank the Wilhelm Frank Trust and the South African Research Chair initiative for their financial assistance throughout the duration of this project.

Stellenbosch University https://scholar.sun.ac.za

Contents

Stellenbosch University https://scholar.sun.ac.za

1 Introduction

The ability to control or change a molecular system, whether it be biological, physical or chemical, using light is a powerful mechanism to have access to. This ability is far reaching, both scientifically and commercially: from the research of fundamental processes such as photo-induced isomerization in photochemistry and the development of new fields such as optogenetics, to the development of nanoparticles for drug delivery, molecular switches, artificial muscles and molecular motors [1, 2, 3, 4]. The challenge here is to find or synthesize the appropriate photo-active molecule that has the desired properties in its reactant and photo-induced state. This property, for example, could be structural, optical or chemical [5]. A molecule designed by Helmy *et al.* in 2014 illustrates this particularly well - in their reactant state, the molecules are coloured and hydrophobic and upon photo-excitation become colourless and hydrophilic [6]. The changes in hydrophobicity of these molecules enable them to act as molecular cargo carriers which release their cargo upon photoexcitation.

The development of molecules such as the one mentioned previously can be based solely on their macroscopic properties without knowing the dynamics of the underlying photophysical processes. However, researching these processes is important for two reasons. Firstly, by studying the dynamics that result from the configuration and profiles of the potential energy surfaces, the forces that are responsible for a particular behaviour, new mechanisms or insights into existing ones can be revealed. Secondly, it can provide the information needed to alter the molecular properties in a specific manner as to obtain a certain result. For instance, with the knowledge of processes that compete with the formation of photo-products or the rate at which they form, alterations can be introduced to modify the yield or rate as required. This type of quantitative information could also be indicative of which applications a molecule may be suited to. In the case of optical limiters for example, the desired response of the molecule/system may be required to occur within an application-specific duration [7].

Of the numerous molecules that display photo-induced behaviour, the group of molecules that are of interest in this study are the metal dithizonate complexes. They typically consist of a transition metal atom which is complexed with a varying number of dithizone ligands. The ligand contains two phenyl rings which are connected via a N = N - C = N - N backbone that hosts a delocalised π-electron system. Certain complexes are reported to display reversible photochromism: they undergo a change of colour when illuminated, and revert back to their reactant form after a period of time [8]. The metal dithizonates have been known about since the 1950s's, but despite this, there have been relatively few studies conducted on them [8]. The studies that are available are primarily involved with determining which of the complexes are photochromic, the mechanism/process driving the photochromism and potential applications [8, 9, 10]. The results were mostly based on what could be inferred from the slow back reaction of certain metal dithizonates (primarily mercury dithizonate). The lack of literature with regards to the photo-induced reaction is mainly due to the fact that femtosecond spectroscopy is required to investigate these processes and it only become available in the 1990's [11]. Recent years however, saw the first ultra-fast transient absorption studies on a single ligand metal dithizonate (dithizonatophenylmercury(II) (DPM)) being conducted by the Ultrafast research group at the Laser Research Institute (Stellenbosch University) led by Prof H. Schwoerer [12]. In 2011 they confirmed the ligand's C=N trans-cis isomerization mechanism that was put forward in earlier literature and revealed that the photo-product forms via a conical intersection at a rate of 1.5 ps. At the conical intersection the reaction pathway is split (50:50) such that the excited state can either return to the ground state or proceed to form

Stellenbosch University https://scholar.sun.ac.za

the product. Further studies were conducted by von Eschwege *et al.* on the same molecule which demonstrated how the dynamics of the isomerization can be altered by incorporating different substituents on the ligand [13]. Depending on the substituent, it was found that the rate associated with the radiationless reaction path through the conical intersection was altered.

This project serves to continue the transient absorption study done by Schwoerer *et al.* by considering metal dithizonates that consist of two ligands and different central metal atoms (Mercury , Zinc, Lead and Nickel). The effect on the dynamics due to the different metals and the presence of a second ligand are of particular interest as they can be compared to the results of DPM. The Dithizone ligand will also be investigated with the hope that it will contribute to unravelling the ultrafast dynamics that occur in the metal dithizonates. To our knowledge, there have been no ultrafast transient absorption measurements performed on these molecules or the ligand. As a consequence of this, the current research can contribute to the fundamental understanding of C=N isomerizations in molecular physics and the molecular dynamics of the metal dithizonates. The latter here, being important if these molecules are to be used in certain applications.

Apart from the investigation of the metal dithizonates, extensive technical work on the setup in the laboratory and existing measurement software (National Instrument's LabView) has been done. LabView is chosen as it offers a convenient way of integrating and controlling different devices as well as the ability to provide full automation of measurement routines. Becoming acquainted with the LabView 'coding' environment and the measurement procedures involved thus form an integral part of this project. Additionally, alternative data analysis techniques namely, global- and global target-analysis will be explored using the Glotaran software package [14]. This will complement current analysis routines.

2 Photochromism and the metal dithizonates

2.1 Photochromism

The onset of a reversible colour change (chromism) in different molecules can be initiated by several different means. Photo-induced chromism (photochromism) is but one type of chromism amongst several which includes thermo-, electro-, salvato- and piezochromism [15]. Photochromism, the type of chromism of interest to this study, is defined as a photo-induced reversible transformation between chemical species that have distinct absorption spectra [5]. The reaction can be written as

$$\text{Reactant} \underset{hv_2,\Delta}{\overset{hv_1}{\rightleftarrows}} \text{Product} \tag{2.1}$$

where the onset of the reaction requires a photon with energy hv_1 and the photo-product returns to the reactant form by means of either photo-excitation with a photon of energy hv_2 (P-type photochromism), or by a thermal pathway Δ (T-type photochromism). In the Spiropyrans for example, both T- and P-types can be present. The Fulgides or Anils on the other hand, display only one type [5]. Although the change in absorption spectra is central to photochromism, there are other reversible molecular and supramolecular properties that can accompany the spectral changes. These properties include, but are not limited to, changes in refractive indices, enthalpy, catalysis, conductivity and solubility [5].

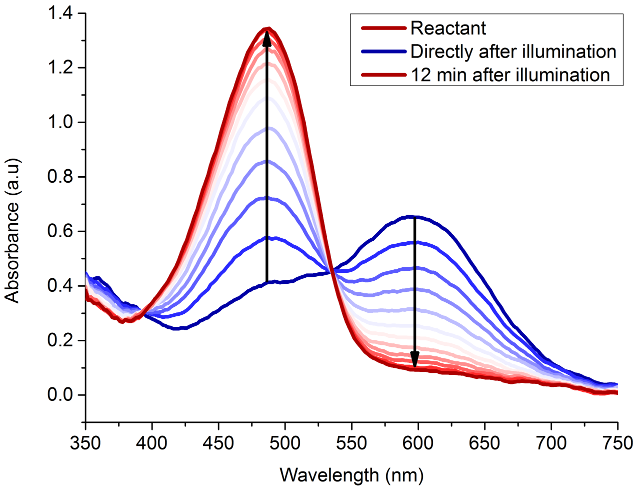

Figure 2.1: Photochromic behaviour of mercury dithizonate in dichloromethane (DCM). The procession of blue → white → red curves show the reverse product → reactant reaction at one minute intervals.

To provide a tangible example of photochromism the absorption spectrum of mercury dithizonate before and after being illuminated with a white light source is examined. This metal dithizonate is known to display T-type photochromism and has a back reaction that typically takes place in the order of seconds to minutes depending on the temperature and solvent. A recent study suggests that it may also exhibit P-type behaviour in polymer films when the

Stellenbosch University https://scholar.sun.ac.za

product is illuminated at 610 nm [9]. Figure 2.1 depicts the spectral evolution at different times after illumination. The reactant's ground state absorption before being illuminated is depicted by the dark red curve and consists of an absorption maxima at 490 nm. Directly after illumination, the curves that follow (blue→white→red) give the spectral profiles at increasing times after excitation. After illumination there is a significant decrease in absorption of the reactant band at 490 nm and the simultaneous appearance of the 600 nm product band [8]. The absorption of the product decreases as time elapses and is accompanied by a rise of the reactant absorption. This is indicative of the thermal reverse reaction where the product returns to the reactant form without the presence of light. The reverse reaction does not contain any intermediaries as evident from the isosbestic point at 535 nm.

2.2 The metal dithizonates

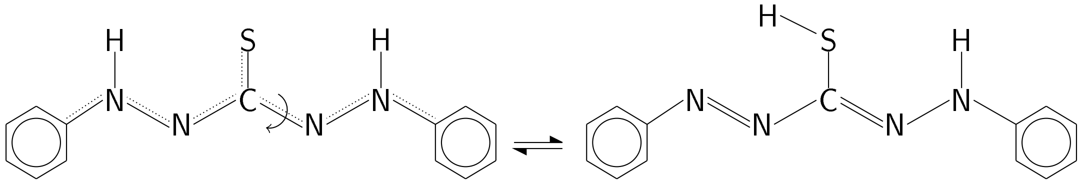

Figure 2.2: The dithizonate ligand in its keto form (left) and enol form (right)

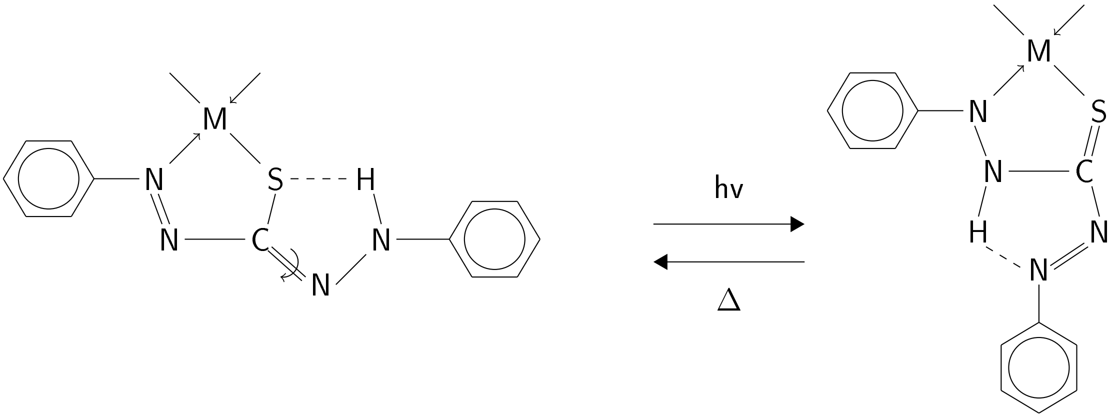

Figure 2.3: The reactant and product structures of M(HDz)$_2$ where M = Hg, Zn, Pb and Ni. The second ligand attached to the metal atom has been omitted for clarity.

Dithizone (diphenylthiocarbazone), an analytical reagent, participates as a ligand when complexed with various transition metal ions to form complexes known as the 'metal dithizonates' [16]. As a consequence of this, it has predominantly been used for colourimetric analysis and detection of trace metals. [8, 17, 18]. Dithizone is reported to be photochromic (in hexane) forming a product with a calculated absorption profile centered around 560 nm, and retains its photochromicity when complexed with various transition metals [19, 8]. The molecule, along with being photochromic, also displays solvato- and concentrato-chromism [16]. Dithizone exists in a tautomeric equilibrium between its keto and enol forms which are shown in Figure 2.2 [20]. Both contain two phenyl rings connected via a chain consisting of carbon and nitrogen, and differ only by the placement of a hydrogen atom on the sulphur. It is interesting to note that the placement of the hydrogen causes a dramatic change in the spectrum of the molecule; the keto form is calculated to have two absorption bands situated at 608 nm and 386

Stellenbosch University https://scholar.sun.ac.za

nm whilst the enol form only has one at 379 nm [20]. The change is associated with the loss of conjugation across the carbon nitrogen chain as can be seen in Figure 2.2. The peak at the longest wavelength is attributed to a transition between the highest occupied molecular orbital (HOMO) to the lowest unoccupied molecular orbital (LUMO) in which sulphur's lone electron pair participates [20]. In solution a peak at 450 nm is also observed and is attributed to the overlap between the keto and enol forms [20]. The spectrum of Dithizone in dichloromethane (DCM) is given by the green curve in Figure 2.4 where two peaks at 610 nm and 445 nm are visible.

The structure of a complex with two dithizone ligands and metal 'M' is shown in Figure 2.3. Depending on the metal present, the reactant either has a tetrahedral or planar geometry. Hg and Zn complexes are known to have distorted tetrahedral geometry whilst the Ni complex is planar [8, 21, 22]. The structure of the photo-product, which is an isomer of the reactant, is also depicted in Figure 2.3. The absorption of a photon by the reactant leads to an isomerisation about the $C = N$ bond as indicated by the curved arrow. Early literature included a nitrogen-nitrogen proton transfer in conjunction with the isomerisation (as shown in Figure 2.3), but a recent computational study on a single-ligand complex showed that this is not necessarily the case as the product structure in which no proton transfer occurs is energetically more favourable [23]. Further details on the isomerisation are discussed in Section 2.2.1

Majority of the pioneering work on the metal dithizonates was conducted in the 1960's by Meriwether *et al.* who studied twenty-four different metal dithizonates in different solvents. Of the twenty-four samples prepared, they found that nine of the complexes were photochromic in certain solvents under continuous illumination. With regards to the samples in this study, this includes the zinc and mercury complexes when dissolved in dichloromethane and the lead complex when tetrahydrofuran is used as the solvent. The status of the nickel-complex along with other metal-complexes in their study are undetermined as the product return times may have been too fast (relative to their temporal resolution) to accumulate an observable product quantity. The different transition metals present in the complexes were found to affect the photochemical stability and the rate at which the thermal reverse reaction occurs [8]. Generally, the effect on the absorption spectra of the complexes is less pronounced. Tetrahedral complexes have one prominent absorption band in the vicinity of 470-530 nm that shows a shift in wavelength depending on the metal present. These absorption profiles in dichloromethane (DCM) can be seen in the top frame of Figure 2.4. The absorption peaks are situated at 490 nm, 515 nm and 530 nm for the Hg, Pb and Zn dithizonate complexes respectively. The similar profiles and location of absorption peaks of the tetrahedral complexes in comparison to the ligand suggests that the transitions are mainly localised on the ligand [24]. In comparing the tetrahedral complexes, it appears that the metal distorts the conjugated system on the ligand leading to different absorption maxima. Although it is not explicitly stated that the Pb complex is tetraherdral in literature, based on the similar absorption spectra to Hg and Zn complexes, it is reasonable to make this assumption.

The spectrum of the Ni complex shown in the bottom frame of Figure 2.4 is considerably different from the complexes shown in the upper frame. This complex has three absorption bands (475 nm, 565 nm and 670 nm) in comparison to the single band of the tetrahedral complexes above 400 nm. The reason for the appearance of these bands is yet to be confirmed although it is thought that the following may offer an explanation: 1) interaction between the π-electron systems on the co-planar ligands, 2) metal to ligand or ligand to metal charge transfers (CT) and 3) d-d transitions localised on the metal [8, 25].

Stellenbosch University https://scholar.sun.ac.za

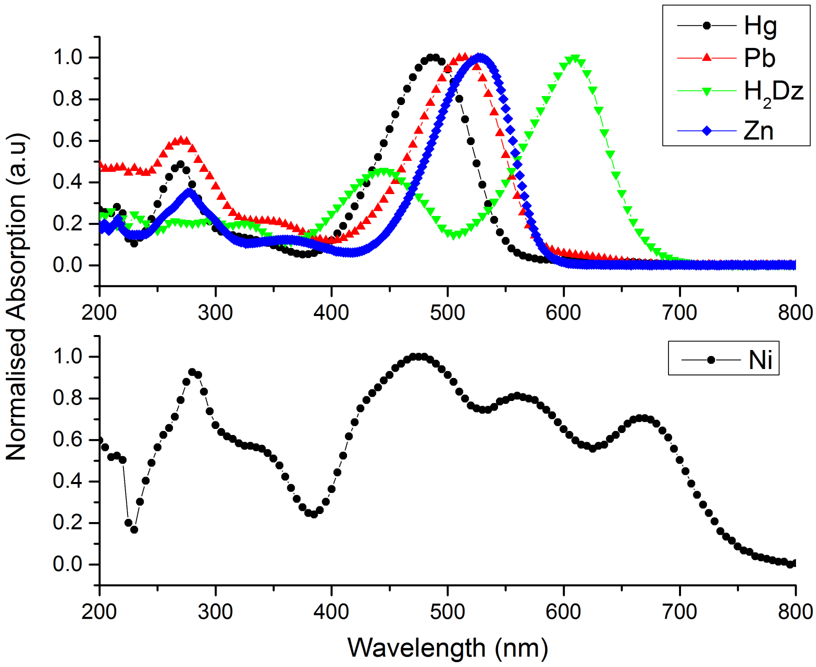

Figure 2.4: Absorption spectra of the tetrahedral $Hg(HDz)_2$, $Pb(HDz)_2$ and $Zn(HDz)_2$ complexes, planar $Ni(HDz)_2$ complex and the ligand H_2Dz.

Of the three possibilities, those presented in 1) and 2) seem most probable. Although there is no literature supporting the claim made in 1), it is reasonable given the square planar geometry at the nickel atom [21]. The d-d transitions should be ruled out as in other less conjugated nickel complexes with sulphur containing ligands the d-d transitions were reported to have a molar absorptivity value in the order of $\epsilon \sim 10^2$ M cm^{-1}. They would consequently not be visible in the spectrum as $\epsilon(\lambda = 475\text{nm}) = 25\ 221$ M cm^{-1}. As for the second possibility it seems likely that the absorption bands can be attributed to metal → ligand CT. In a study conducted on the spectra of planar Nickel complexes containing ligands with a conjugated π system, it was found that for metal → ligand CT, three closely spaced bands that decrease in intensity can be expected [26]. Each of these bands are associated to transitions with the same final state. Further support to associate these bands to charge transfer from the metal to the ligand arises when one considers that the addition of nitrogenous bases to Nickel dithizonate causes the complex to exhibit an absorption spectrum similar to the other metal dithizonates, with only one absorption band (520-535 nm) [25]. This was explained by the 'removal' of an orbital from the metal (upon bonding with the N-base) that is required to form the charge transfer bands with the ligands' π system.

Stellenbosch University https://scholar.sun.ac.za

2.2.1 Ligand isomerisation

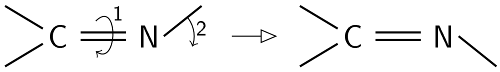

Figure 2.5: 1) and 2): Rotational and inversional isomerisation in Formaldimine. Although both mechanisms are depicted here, it is believed that the rotational mechanism is energetically more favoured [27].

There are roughly six mechanisms/processes which are found in photochromic molecules. Of the six, which include processes such as intramolecular group transfers and redox reactions, the one of interest is an imine isomerisation [15]. Due to the presence of a nitrogen atom in the double bond, the isomerization mechanism is comparatively more complex than to that of a $C = C$ isomerisation [28]. The complexity arises from the molecular orbital transitions that have to be considered and the motion that can occur during the isomerization. Along with the bonding to anti-bonding transition ($\pi \rightarrow \pi^*$), non-bonding to anti-bonding transitions ($n \rightarrow \pi^*$) also have to be taken into account due to the lone electron pair on the imine nitrogen. With regards to the motion, it can take place by means of two linearly independent mechanisms, namely twisting/rotation and in-plane inversion [29]. These two motions can be seen in Figure 2.5 where the first motion depicts rotation and the second, inversion. There is also speculation that the mechanism may not necessarily consist purely of one or the other, but as a linear combination of the two [29]. The type of motion that occurs depends largely on the atoms/functional groups that are attached to the imine carbon and nitrogen atoms and whether they strengthen or weaken the double bond character of the transition state [30]. As the $C = N$ bond in the ligand is part of a larger chain, by looking at the attached groups a conclusion cannot be drawn, however, a recent computational study suggests that the twisting path is favoured [13]. The calculated LUMO and HOMO show that the double bond between the carbon and nitrogen is diminished to a single bond upon photo-excitation, and thus allows rotation to occur.

The presence of two ligands that can photoisomerise in certain metal dithizonates presents certain ambiguities with regards to whether isomerisation occurs in both ligands or only in one. The probable scenarios which may arise upon absorption of a photon are shown in Figure 2.6 and are as follow: 1) isomerisation of a single ligand; 2) simultaneous isomerisation of both ligands; 3) stepwise isomerisation.

$$1 \quad \text{R-Hg-R} \xrightarrow{\text{hv}} \text{P-Hg-R} \qquad 2 \quad \text{R-Hg-R} \xrightarrow{\text{hv}} \text{P-Hg-P}$$

$$3 \quad \text{R-Hg-R} \xrightarrow{\text{hv}} \text{P-Hg-R} \xrightarrow{?} \text{P-Hg-P}$$

Figure 2.6: Three possible isomerisation schemes in the two-liganded metal dithizonates. ‘R’ and ‘P’ refer to whether the ligand is in its reactant or product state respectively.

Insights with regards to 1) can be gained by comparing $Hg(HDz)_2$ to the single-liganded complexes shown in Table 2.1. The side chains and different substituents on the single-

Stellenbosch University https://scholar.sun.ac.za

Table 2.1: Absorption maximum and molar aborptivities of single- and double-liganded metal dithizonate complexes

Sample	Wavelength (nm)	ϵ M cm^{-1}	Solvent	Source
$Hg(HDz)_2$	498	102 564	Chloroform	[31]
	498	71794	DCM	[31]
	485	70 500	Chloroform	[32]
	490	63 400	DCM	Communication with Prof. K. von Eschwege
Hg(HDz) with Hg-R substituents	470-480	38 000-48000	Chloroform	[32]
Long chain Hg(HDz) (Azomethine series)	484-487	35 500-42 000	Chloroform	[33]
DPM	470	57 300	Hexane	[23]
DPM	470	35 000	Chloroform	[32]
o-methoxy DPM	505	28 300	DCM	[13]

liganded complex's Hg atom do not play a role here. The similar absorption maxima bear witness to this as well as the molecular orbital renderings of DPM's product and reactant forms; in the reactant form there is no 'contribution' from the Hg atom or the phenyl and only a minimal contribution from the Hg atom in the product. The spectral profiles of the reactant forms of all the complexes are virtually identical with the absorption maxima of the reactants differing only by a couple of nanometers. As before with the different metals present, the spectral similarity of the complexes would suggest that the photo-induced transition remains localised on the dithizone ligand. Given all of the above, any differences between the complexes should thus exclusively be attributed to the presence of a second ligand. If the ligands act as independent absorbers the molar absorptivities of the complex with the two dithizonate ligands should be roughly double that of the single-liganded complexes. The values listed in Table 2.1 appear to confirm this. There is thus strong evidence to believe that the ligands are independent and only one ligand isomerises upon excitation.

Considering the absorption spectrum of $Hg(HDz)_2$, $Zn(HDz)_2$ and $Pb(HDz)_2$ alone, scheme 2) should be disregarded. For both ligands to isomerise simultaneously a coupling between them across the Hg atom would be required. This is unlikely due to the tetrahedral geometry around the metal, but supposing that the two ligands were coupled, it is highly improbable that the absorption spectrum should remain similar to that of DPM or other single-liganded complexes. The other option available to describe scheme 2) would be two-photon absorption. Although $Hg(HDz)_2$ does display nonlinear optical properties, it is improbable that two-photon absorption played a role in any of the studies due to the high intensities required.

In support of the third scheme where both ligands isomerise, a continuous photolysis study on $Hg(HDz)_2$ obtained a quantum yield value close to unity[1] [34]. Although the authors of this study claim that scheme 2) is appropriate, their study was insensitive to changes on ultrashort timescales and under continuous photolysis, isomerisation of both ligands can be expected (if they act independently). Assuming that both ligands are in their product form after photo-excitation and ruling out simultaneous isomerisation, the only alternative is the mechanism shown in 3) which supports a stepwise mechanism where isomerisation of one ligand leads

---

[1] In obtaining this value however, an assumption about the fraction of product formed is made which may or may not necessarily be correct.

Stellenbosch University https://scholar.sun.ac.za

to a secondary isomerisation. In a photolysis study in ethanol, where the product was visible immediately after a 35 ps pulse, a two-step process was not supported by the data at times between 35 ps and 5 ns. It is worthy to mention that in their data, after 5 ns, an increase of 30% in the absorption at 600 nm was observed and a decrease in the 490 nm bleaching signal. In the event that the second ligand isomerises, a rise in the product absorption should be seen as well as an increase in the bleaching. Knowing that the DPM product forms within 1.5 ps would thus suggest that a secondary isomerisation may occur on either a time scale between 1.5-35 ps or on a longer nanosecond scale. Mechanisms which may account for a stepwise mechanism are either inter- or intra-molecular charge transfer, the latter not being in favour due to the molecular geometry.

At this point, we thus have that either scheme 1) or 3) remain as possibilities. However, as the only literature containing information on dynamics in the ultrafast regime of the metal dithizonates is on DPM, DPM will serve as the initial model that will be consulted. In other words, it is assumed that the isomerisation depicted in scheme 1) is valid. We also note that measurements done exclusively on the dithizone ligand can be compared to those of the metal dithizonate complexes. This should provide clarity in terms of which scheme is favoured depending on the dynamics that are observed in each.

3 Transient Absorption Spectroscopy

3.1 An overview

To study the photo-induced behaviour of the metal dithizonates, the temporal evolution of underlying molecular dynamics, which includes possible processes such as intersystem crossing, internal conversion and vibrational relaxation are investigated. As these processes occur on a femto- to pico-second time scale, conventional electronic detectors cannot be used to follow their temporal evolution due to their limited response times [29]. A method which offers a work-around for this complication is a pump-probe spectroscopic technique known as Transient Absorption Spectroscopy (TAS) [11].

In a TAS measurement, given an ensemble of molecules, a 'pump' pulse is used to excite a fraction of the molecules into their excited state. Following this, a spectrally broad pulse (known as the 'probe' pulse) with a controllable delay is sent through the molecular ensemble at varying times with respect to the pump pulse in order to capture the transient absorption spectrum of the ensemble. This pulse allows the states that have either been populated or depopulated, as a consequence of the pump pulse, to be monitored at different times. In delaying this pulse incrementally from the time it overlaps with the probe pulse, spectra of the altered probe pulse can be gathered in time 'frame by frame' to produce a full picture of the dynamics that occur. As the fraction of molecules that are typically probed is in the order of a percentage, to increase the sensitivity to the changes in the probe pulse the data is described using the change in optical density (ΔOD) [11]. The ΔOD is given by:

$$\Delta\text{OD}(\lambda, \tau) = -\log\left(\frac{T_p}{T}\right) \tag{3.1}$$

where $T_p = 10^{-(OD)_p}$ and $T = 10^{-OD}$ (by the Beer-Lambert law) are the sample's pumped and unpumped transimission values respectively and τ is the delay between the pump and probe pulses. Note that by this definition the sensitivity to changes of the probe beam is increased due to the removal of the spectral contribution from the unpumped molecules.

3.2 Transient Spectra

To illustrate how the $\Delta\text{OD}(\lambda, \tau)$ dataset is visualised as a transient absorption spectrum and the information it provides, results from the ultrafast study on DPM (pumped at 480 nm) are shown in Figure 3.1a. To compliment the transient spectrum and aid in explaining the origin of the signals in the spectrum, the postulated model is also shown (Figure 3.1b). The spectrum in Figure 3.1a displays ΔOD on a colour mapped z-axis as a function of wavelength (y-axis) and time (x-axis). The positive and negative values taken on by Equation 3.1 are translated in the colour map by the use of red and blue respectively - red regions thus indicate an increase in absorption (or a decrease in transmission: $T_p<T$) through the sample, and blue values a decrease (or an increase in transmission: $T_p>T$). Green regions indicate a value of zero where there is no difference between the pumped and unpumped spectra.

In order to illustrate the origins of signals that occur in a transient spectrum, the transient spectrum of DPM along with the postulated model and potential energy surfaces are shown in Figures 3.1b and 3.1c [12]. Physically, the model is interpreted as a fast radiationless decay from an excited reactant state (R^*) to a transition state (TS) which can either decay back

Stellenbosch University https://scholar.sun.ac.za

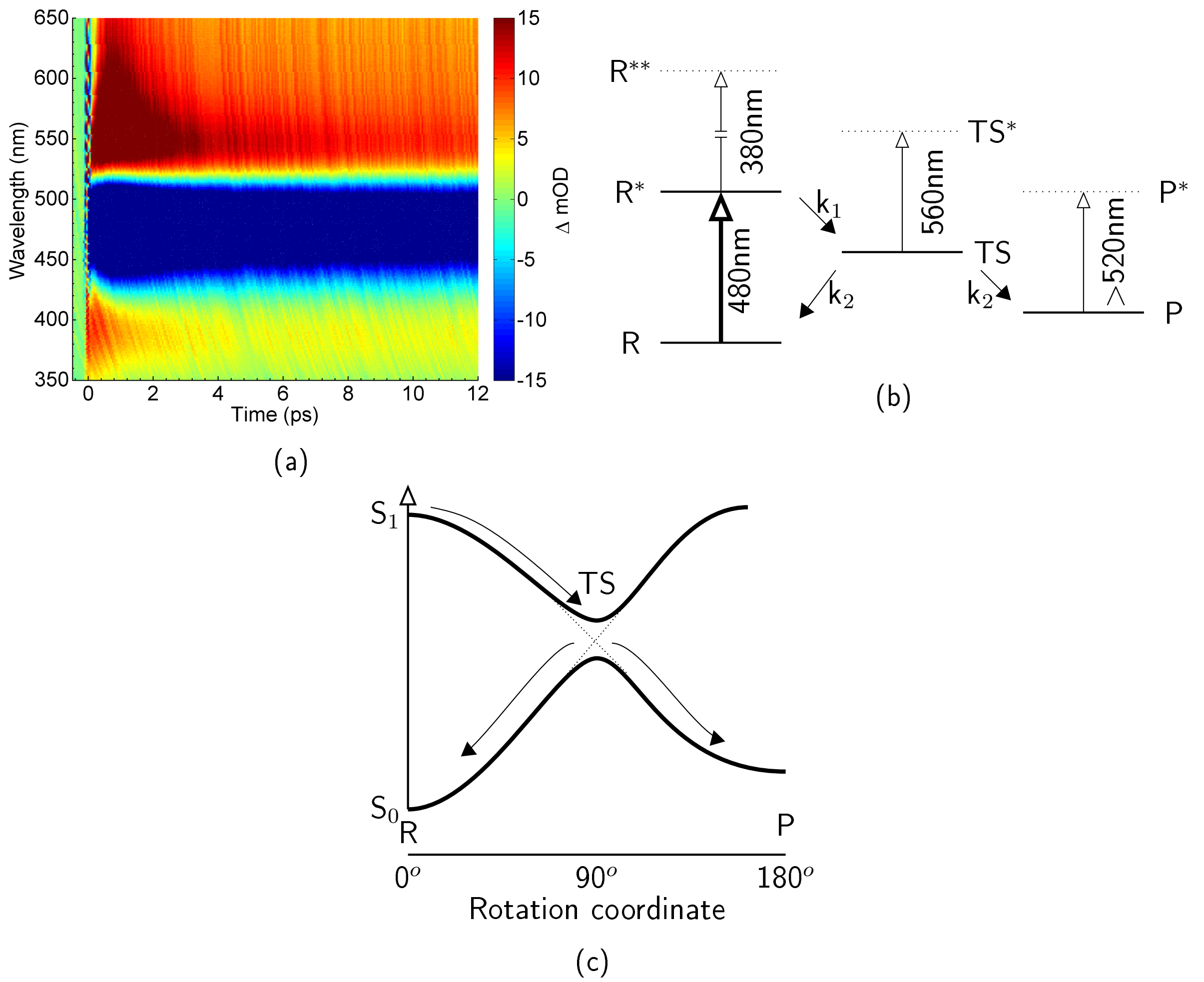

(a)

(b)

(c)

Figure 3.1: A transient absorption spectrum of dithizonatophenylmercury (DPM) along with the molecular model that was postulated [35]. b) and c): The molecular model shown in terms of a kinetic scheme and potential energy surfaces.

to the ground state (R) or the product state (P) with equal probability. The R* →TS decay represents a twisting/rotation of the C=N from $0^o \rightarrow 90^o$ to yield an orthogonal intermediate state. Once in the orthogonal geometry, the rotation can either continue to 180^o which yields the product form, or rotate back to 0^o resulting in the reactant form.

There are four different signals that arise from the molecular photo-reaction in a transient spectrum: 1) ground state bleaching; 2) stimulated emission; 3) excited state absorption; 4) product absorption[1]. When excitation at 480 nm occurs, electrons are promoted from their ground state R to an excited state R*. This results in an instantaneous appearance of two signals: a positive signal centered around 380 nm and a negative signal at 480 nm. The negative signal contains a contribution from the ground state bleach (GSB) and stimulated emission (SE). The GSB is present due to the pump-pulse reducing the number of molecules that are in their ground state. As the ensemble contains both unpumped and pumped molecules, after excitation there are less molecules in the ground state and thus a decrease in absorption occurs at the pump wavelength. The stimulated emission occurs due to the probe-pulse stimulating

---

[1] Note that as a molecular ensemble is considered, these signals represent a superposition of 'signals' from individual excited molecules and thus reference to 'electrons' or 'electron population' in the discussion that follows refers collectively to all electrons that were excited in the ensemble and not multi-photon processes in individual molecules.

Stellenbosch University https://scholar.sun.ac.za

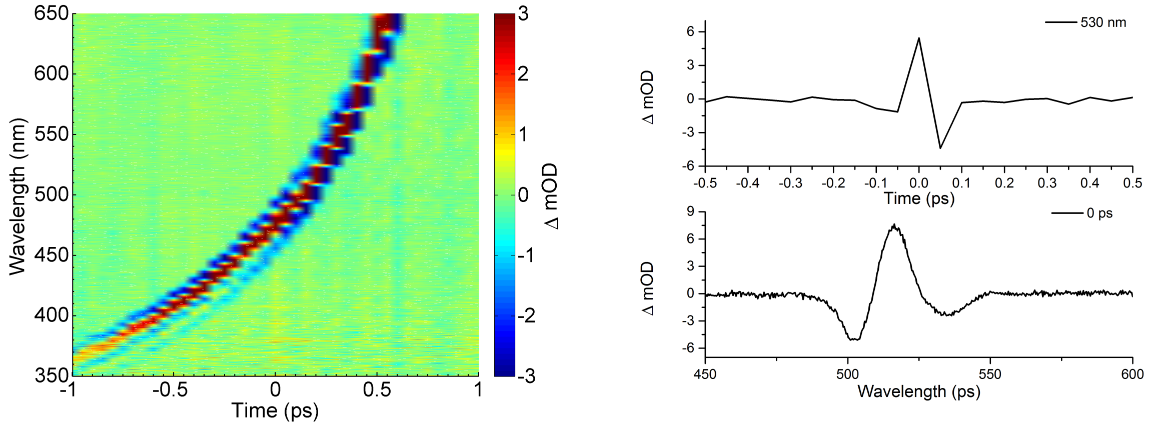

(a)

(b)

Figure 3.2: a) Coherent artefact present in liquid phase transient absorption spectra (dichloromethane). b) Spectral and temporal lineouts of the coherent artefact

a transition from the now occupied R* state, to the ground state. The population of the R* state is not significantly affected by this as the probe-beam is considerably weaker than the pump-pulse. The instantaneous positive signal that appears is due to electrons in R* absorbing the probe beam and transitioning to a higher energy state R**. This is known as instantaneous excited state (IES) absorption (IESA). Non-instantaneous excited state absorption (ESA) occurs from states which have been populated as a result of transfer from the R* state. This can be seen in the transient spectrum above 560 nm which represent TS → TS* absorption. The last signal, product absorption, occurs as a long lived positive absorption through out the spectrum due to P→ P* absorption. Evidence of the product can be seen in the spectrum at 350-410 nm and the broad region above 520 nm where the signal remains constant after the initial dynamics.

The Coherent Artefact

At time zero in Figure 3.1a an obtrusive signal which is not related to the molecular photoreaction is visible. For clarity, it is shown in Figure 3.2. This signal is a coherent artefact that stems from cross-phase modulation of the pump and probe pulses in the cell and/or solvent used in liquid phase transient spectroscopy. The intense pump beam introduces a time-dependent change in the refractive index of the flow cell and/or solvent which then causes a time-dependent modulation of the probe pulse's phase and spectrum [36]. Although the artefact can distort the data at early times, it can be used to determine the wavelength dependent temporal overlap of the pump and probe pulses. The wavelength dependence of the overlap results from the chirp in the white light probe pulse (see Section 3.4).

Stellenbosch University https://scholar.sun.ac.za

3.3 Obtaining Transient Spectra

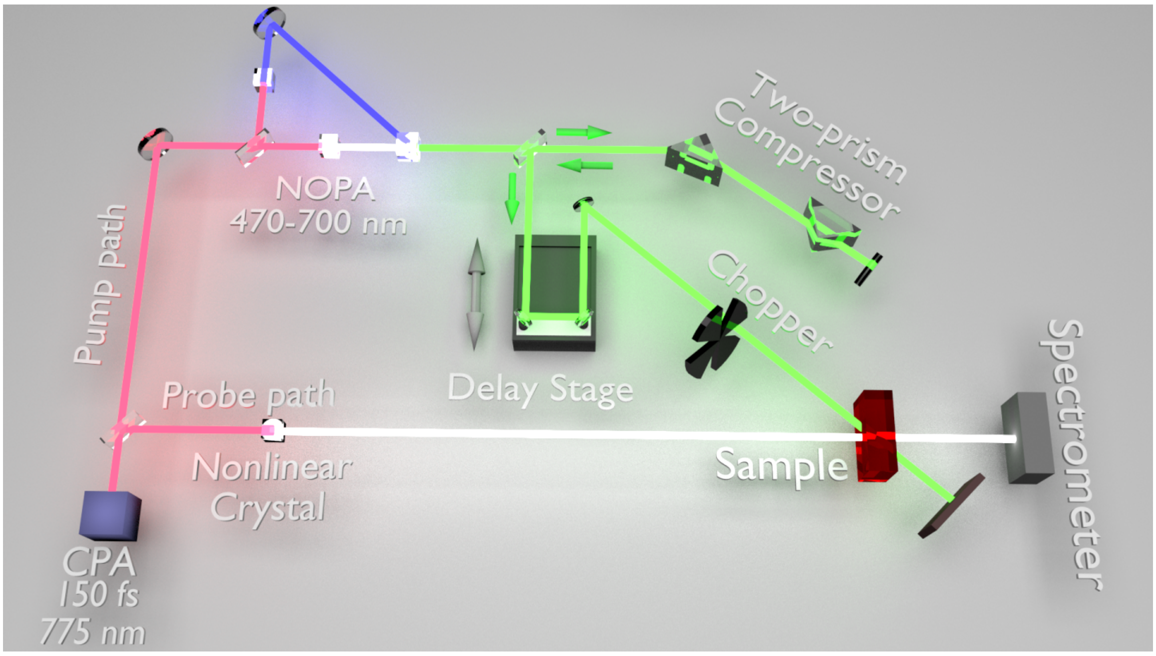

Figure 3.3: Experimental setup at the LRI. For clarity, not all optical components are shown.

The primary components in a transient absorption measurement are the pump and probe pulses. The setup is thus considered in two halves: one pertaining to the generation of the pump pulse, and the other the probe pulse. Both pulses are generated using the same laser source: a Ti:Sapphire chirped pulse amplifier (CPA) with a repetition rate of 1 kHz, central wavelength of 775 nm and pulse lengths of $\sim$ 150 fs. Upon exiting the CPA, the beam is split into the pump and probe paths which are illustrated in Figure 3.3.

The spectrally broad probe beam is generated by sending the fundamental through one of three different nonlinear crystals. Prior to entering the crystal, the beam goes through a half-wave plate set at the magic angle of 54.7^o relative to the pump pulse. This eliminates contributions to the spectra from the rotational reorientation of the pumped sample. The different crystals used to generate the supercontinuum provides different spectral ranges that enables probing in the ultra-violet, visible and near infrared (see Section 3.4). Calcium Fluoride (CaF_2), Sapphire and Yttrium aluminium garnet (YAG) crystals are used for the aforementioned spectral regions respectively. Upon exiting the crystal, the white-light beam is reflected by an off-axis parabolic mirror which collimates it and a filter that removes the 775 nm fundamental. The white light is focused onto the sample and a second lens used to collimate the beam afterwards. The light then enters an optical fibre which is coupled to an Andor SR163 spectrometer. Attached to the spectrometer is a 1024 pixel line scan camera (Entwicklungsbüro Stresing) used to capture individual white light spectra, pulse by pulse. In a typical measurement 6000 pumped and un-pumped spectra are captured for each pump-probe delay time (further details on the measurement procedure and software are given in Appendix B.2).

Stellenbosch University https://scholar.sun.ac.za

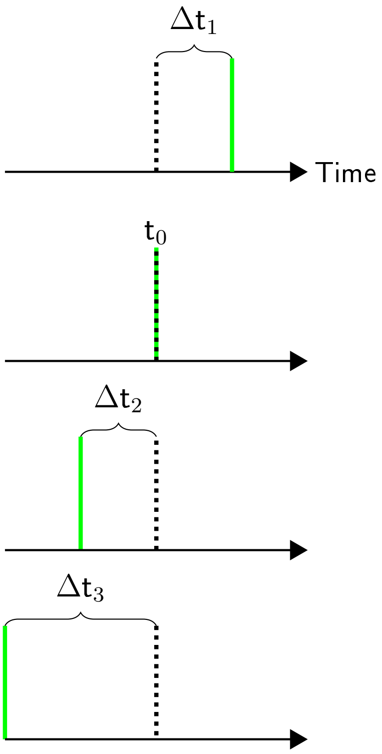

Figure 3.4: A depiction of how the delay between the pump and probe pulses is changed during the course of a measurement. The dotted line represents the probe pulse and the green line the pump pulse.

Since the excitation wavelength may vary from sample to sample, the pump pulse is required to be tunable. To provide this capability a non-collinear optical parametric amplifier (NOPA) is employed, which can provide pumping wavelengths between 470 nm and 700 nm (see Section 3.5). After exiting the NOPA the pulses are compressed temporally using a two-prism compressor to pulse durations below 50 fs. Next, the probe beam is sent to a 10 cm mechanical delay stage which controls the delay of the pump pulse's arrival time at the sample (relative to the probe pulse's). As the delay stage is set up in reflection, the maximal displacement of the stage translates to a temporal domain that spans roughly 660 ps. The reason for changing the delay of the pump instead of the probe is that it is experimentally more pragmatic; steering of the spectrally broad probe pulse over long path lengths would require that the increased dispersion be compensated for. In Figure 3.4 the relative arrival times of the pump and probe beams at the sample are depicted. Here we see the probe pulse arriving at a fixed delay relative to the probe pulse and the delay time Δt_i between the pulses increasing. The delay stage is used to incrementally shorten the path traversed by the pump beam causing it to arrive earlier each time. Consequently, transient spectra are recorded at increasing times after the initial excitation. The overlap of the two pulses marks the beginning of the signal (t_0 or 'time zero') as indicated in Figure 3.4.

A chopper operating at 500 Hz is introduced into the pump's beam path prior to the sample to block every second pulse. This is done to produce alternating pumped and un-pumped spectra. After leaving the chopper, the pump beam is overlapped both temporally and spatially with the probe beam on the sample. The spatial alignment is done by aligning the two beams through a pinhole with a diameter of roughly 50 μm. Note that the pump pulse is aligned non-collinearly on the sample relative to the probe to minimise scattering into the detector. Temporal alignment is required to determine whether the pump and probe beams will overlap within the range available on the translation stage. To adjust this, the path length of the probe pulse is altered.

To determine how the sample will be introduced into the measurement, the sample's return rate to its un-pumped state and the laser's repetition rate must be taken into consideration. If the sample returns to its un-pumped state after being pumped before the next probe pulse arrives (after 1 ms), there is no need to replace the sample in between pulses. However, if the return rate is more than the time between consecutive pulses, an un-pumped sample needs to be introduced between pulses. Supposing that this was not done, erroneous data would be obtained as the excited state of the sample would be pumped and probed. Because at least one of the samples had a return rate orders of magnitude larger than the time between pulses, a flow cell was required to evacuate the ensemble of pumped molecules and introduce an un-pumped sample prior to each pump pulse. The samples were originally provided in crystal form

Stellenbosch University https://scholar.sun.ac.za

and were dissolved in dichloromethane (DCM) to yield concentrations that resulted in 80-90 % transmission. DCM was chosen as the solvent as all the samples are soluble in this medium and the study by Schwoerer *et al.* was conducted in this solvent [12]. The concentrations were calculated using the Beer-Lambert law where the path length was taken as 200 μm. Having a transmission value in this range is important to avoid non-linear effects whilst still maintaining a good signal to noise ratio [35]. A pump fluence of roughly 500 μJ/cm^2 was used.

The closed-loop flow cell can be seen in Figure 3.5. An in-line rotary pump (HNP Mikrosysteme GmbH: MZR 2921) is used to pump the liquid sample from a reservoir through the flow cell and back to the reservoir. Teflon tubing is used to connect the different components as to avoid reacting with the solvent used. The rate at which the sample was pumped through the system was done in accordance to the parameters specified by Bosman [35].

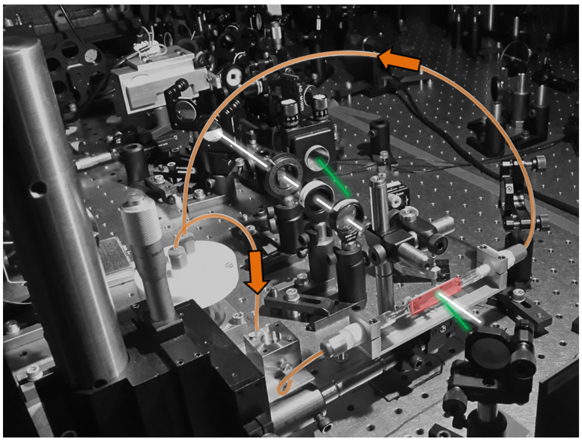

Figure 3.5: Closed-loop flow cell. The sample is pumped (from left to right) from the reservoir to the flow cell (indicated in red) where the pump and probe beams are overlapped (green and white lines respectively). The pumped sample is then evacuated and proceeds back to the reservoir.

3.4 The white light probe pulse - Generating a Supercontinuum

Broadly stated, white light generation (WLG) or supercontinuum generation (SCG) occurs when an ultrashort pulse with sufficient power traverses through a transparent medium [37, 38, 39]. It can occur in a variety of nonlinear media including solids, gases or liquids [39]. After travelling through the medium the pulse's spectrum is significantly broadened to form a supercontinuum. The mechanisms that lead to WLG are not yet fully understood as the spatial and temporal coupling of the numerous processes involved make it an inherently complex phenomena [39]. This has led to various mechanisms being put forward. The most prominent of these are self-focusing and self-phase modulation (SPM) which originate from nonlinear (NL) optical processes. When an optical field is incident on a medium, its electric field $E(t)$ causes a time dependent polarisation $P(t)$ of the medium which ultimately leads to NL processes. The response of the medium to the electric field is governed by its susceptibility and is describe by

$$P(t) = \epsilon_0 \left(\chi^{(1)}E(t) + \chi^{(2)}E^2(t) + \chi^{(3)}E^3(t) + \dots\right) \tag{3.2}$$

where $\chi^{(n)}$ is the n^{th} order susceptibility. As the crystals used in this study are centrosymmetric, the lowest order NL contribution comes from the third order term. The third order term is responsible for causing an intensity dependent refractive index which is described by $n = n_0 + n_2 I$ where n_0 and $n_2(\chi^{(3)})$ are the linear and nonlinear indices of refraction respectively. This in turn leads to the phenomena of self focussing and self-phase modulation mentioned earlier.

Self-focusing is a process whereby the incident light modifies the medium in such a way that it acts as a lens and causes the beam to become focused within the medium [40]. For self-focusing to occur it requires that the pulse power exceeds P_{crit} which is dependent on the pulse's wavelength and the medium (n_0 and n_2). The pulse's self-focus diameter is limited by processes which compete with the intensity dependent refractive index. These processes include free electron generation and diffraction which causes a negative change in the index of refraction and competes with the $n_2 I$ term [37].

SPM occurs due to the laser pulse's temporal nonlinear phase distribution [37]. An indication of the spectral composition of the pulse is given by considering the instantaneous frequency, ω, which is described by

$$\omega = \frac{d\phi(t)}{dt} = \omega_0 - \frac{d\phi_{nl}(t)}{dt} = \omega_0 - \frac{n_2 L \omega_0 \dot{I}(t)}{c} \tag{3.3}$$

where L is the propagation distance, ω_0 the central frequency and $I(t)$ the intensity. This indicates that the spectral content depends on the rate of change of the pulse's intensity. If it is assumed that the laser pulse's intensity is represented by a Gaussian distribution then from Equation 3.3 we note that the pulse will be red shifted in the front and blue shifted at the back - the 'red' components form in the leading edge of the pulse, and the 'blue' components in the trailing edge. Furthermore, if group velocity dispersion is taken into consideration, the spectral components will also acquire a temporal rearrangement leading to a chirped continuum - in other words, the pulse is stretched out temporally. This can clearly be seen in the transient spectrum in Figure 3.6b where the shorter wavelengths arrive first. The reason that the shorter wavelengths arrive first in the spectrum, and not the longer wavelength components, results from the way in which the pump and probe beams are overlapped. The chirp in the spectrum is corrected for by fitting a polynomial (as shown by the black curve) and adjusting the data accordingly such that all spectral components coincide with a single time zero. In Figure 3.6 the white light spectra obtained from two different crystals is depicted. The spectrum produced by CaF_2 extends from the ultraviolet (350 nm) to roughly 700 nm where as the spectrum obtain by using Sapphire initially starts at 480 nm and extends beyond 700 nm. The reason for the difference in spectral ranges produced by the two crystals is due to their differences in band gap energy [41]. The abrupt end of the spectrum produced by the CaF_2 above 700 nm is due to the spectrometer's range at a given grating position. The Sapphire's spectrum also ends close to 700 nm, however, this is due to the high-cut filter used to block the fundamental.

Stellenbosch University https://scholar.sun.ac.za

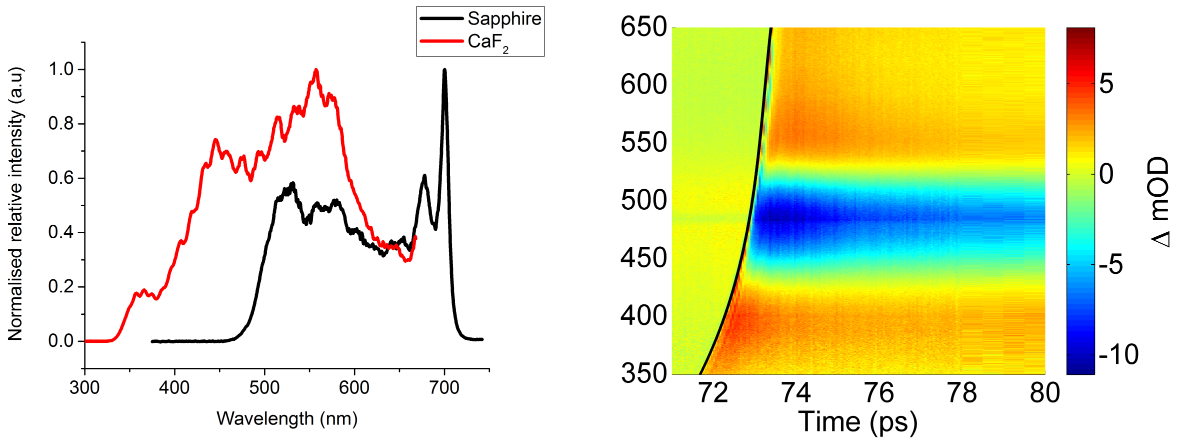

(a) (b)

Figure 3.6: a) White light continuum generated in CaF_2 and Sapphire crystals. b) Fitting the chirp in a transient absorption spectrum.

3.5 The NOPA - Generating a pump pulse

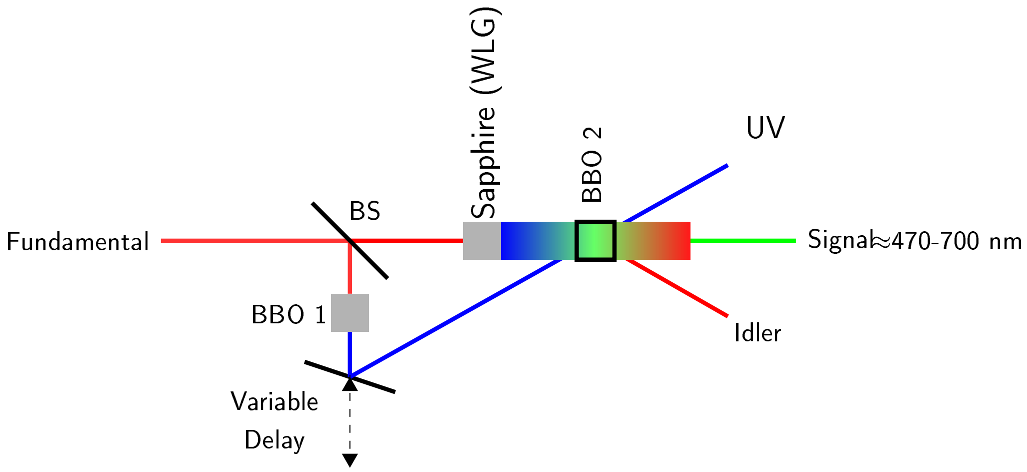

Figure 3.7: A non-colinear optical parametric amplifier

In Figure 3.7 the structure and operation of a NOPA is depicted. The 775 nm fundamental from the CPA is first passed through a beam splitter to yield two paths: one path is frequency doubled (FD) by means of a beta-Borium borate (BBO) crystal and the other is passed through a sapphire crystal to generate a positively chirped SC. These two beams are then overlapped spatially and temporally within another BBO crystal to produce the desired signal. As the white light is chirped, the portion of the SC that is amplified depends on where the FD beam temporally overlaps. A tunable delay stage is placed in the path of the FD beam to allow the FD pulse to overlap at a specific temporal region of the chirped SC. The process by which a tunable output is generated within the BBO is a nonlinear process known as difference frequency generation (DFG) or parametric amplification. If two beams with different frequencies ω_p and ω_s ('pump' and 'seed' frequencies respectively) are incident on a

Stellenbosch University https://scholar.sun.ac.za

second-order nonlinear crystal it is required, by energy conservation, that $\omega_p = \omega_s + \omega_i$ where ω_i is the frequency of the generated idler. This is shown schematically in Figure 3.8.

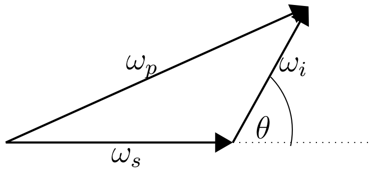

Figure 3.8: Phase matching for DFG

Furthermore, momentum conservation requires that $\mathbf{k}_p = \mathbf{k}_s + \mathbf{k}_i$. This is known as a phase matching condition and implies that the generated pulse will maintain a constant phase relation to the polarisation of the medium and hence the energy is extracted most efficiently. The phase matching condition in this case places a constraint on the angle θ, which is the angle between the signal and idler pulses (as shown in Figure 3.8). Mathematically, this translates to $v_i \cos\theta = v_s$ where v_i and v_s are the group velocities of the idler and signal pulses respectively [42]. Experimentally, this is achieved by changing the angle between the seed and pump pulse and the orientation of the crystal.

Figure 3.9 depicts a selection of pump wavelengths generated by the NOPA. Although the spectra have been normalised for clarity in Figure 3.9, the intensity of the signals depend on the 'amount' of white light present to seed the amplification and the spatial overlap of the pump and seed beams. The spectral content of the SC thus determines the tunability of the NOPA - with a Sapphire crystal a signal between 470 nm and 700 nm can be obtained. In Figure 3.9 one can also see that the signal pulses broaden spectrally at increasing wavelengths due to group velocity dispersion. This, however, is not problematic and allows for greater temporal compression of the pulse (see Sections 3.6 and 3.7).

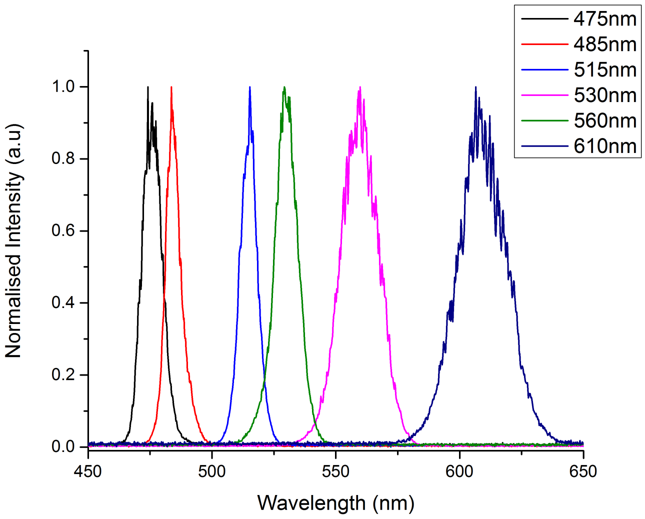

Figure 3.9: Spectral profiles of the pump beam at different wavelengths

Stellenbosch University https://scholar.sun.ac.za

3.6 Pulse compression

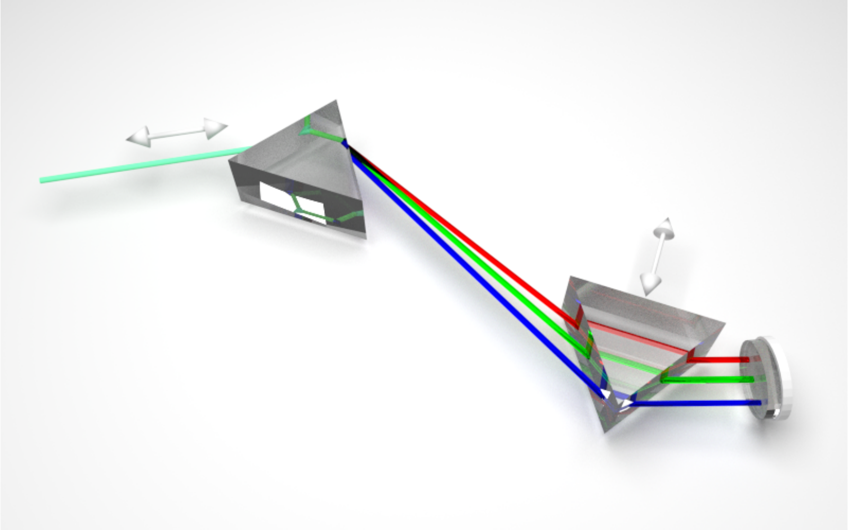

Figure 3.10: Two-prism pulse compressor

Upon exiting the NOPA, the pump pulse's duration is not short enough to meet the temporal requirements of the measurement. To compress the pulse temporally, a two-prism compressor as shown in Figure 3.10 is implemented. The pulse from the NOPA has a positive chirp which implies that the longer wavelength components (red components) of the pulse arrive earlier in time relative to the short wavelength components (blue components). Hence, to shorten the pulse, a negative chirp is applied to the pulse - this allows for the blue components to 'catch up' to the red components, and the red components delayed to 'catch up' to the blue components. This is illustrated in Figure 3.11 where a delay of Δt is applied to the blue and red components.

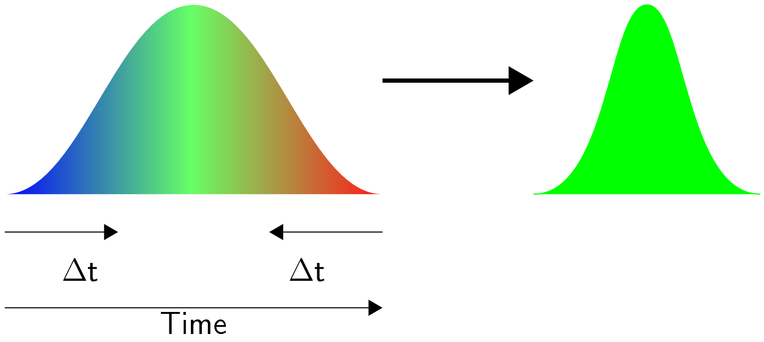

Figure 3.11: Pulse compression using a two-prism compressor.

The pulse is sent to the first prism and aligned such that it is incident at the Brewster angle. Due to the wavelength dependent index of refraction of the prism, the pulse's spectral components are split spatially before reaching the second prism. As the second prism's base is parallel to that of the first prism, the emerging beam is collimated. It is then passed to a mirror which reflects the beam back through the prisms with a slight vertical offset. The vertical shift is required to separate the incoming uncompressed pulse and outgoing compressed pulse. The negative chirp that is applied to counter the positive chirp of the pulse is a result

Stellenbosch University https://scholar.sun.ac.za

of the different times it takes for the components to traverse through the compressor. The 'blue' components travel a shorter path relative to the 'red' components thus allowing them to catch up to the 'red' components and the 'red' components travel a longer path relative to the 'blue' components. The depth of the second prism can be controlled and will consequently determine the induced delay between the components. By adjusting this depth as well as the distance between the tips of the two prisms the pulse can be compressed to below 50 fs.

3.7 Autocorrelation - Determining the duration of a pulse

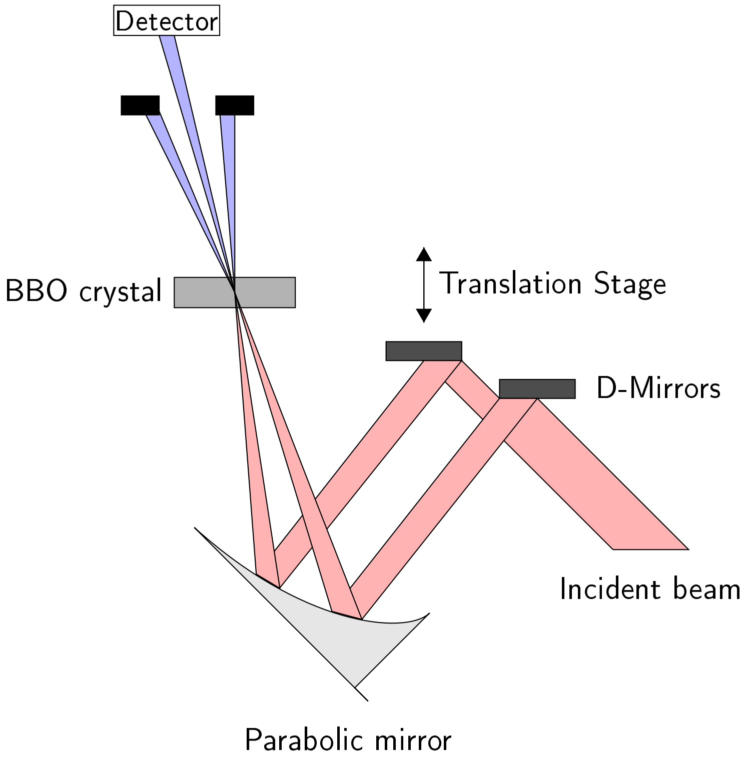

Figure 3.12: The setup of the autocorrelator

To measure the temporal duration of the pump beam after compression, an autocorrelation is taken using the setup depicted in Figure 3.12. The beam (frequency ω) is first split by using two D-shaped mirrors, one of which is attached to a translation stage, and then steered to an off-axis parabolic mirror. The translation stage is used to control the path length of one of the beams and consequently creates a time difference of τ between the two beams. The parabolic mirror then focuses the two beams in a non-linear BBO crystal where frequency doubling occurs - the crystal is mounted such that it can be easily rotated to achieve the correct phase matching angle required at different wavelengths. Both incident beams are frequency doubled and emerge in the direction that they were originally traversing.

Provided that the beams are spatially and temporally overlapped and that the BBO crystal is at the correct phase matching angle, a third 2ω beam is produced at the BBO crystal. This is the autocorrelation pulse and is composed of one ω photon from each of the incident beams. Due to momentum conservation, it appears between the other two frequency doubled beams -

Stellenbosch University https://scholar.sun.ac.za

this is convenient from an experimental standpoint as the beam can be monitored exclusively and allows for a background-free measurement. The autocorrelation pulse is coupled into a optical fibre which sends the light to a photomultiplier tube and the intensity monitored as a function of the temporal difference between the two pulses. An example of this intensity distribution can be seen in Figure 3.13 where the intensity was monitored for an input beam of 490 nm.

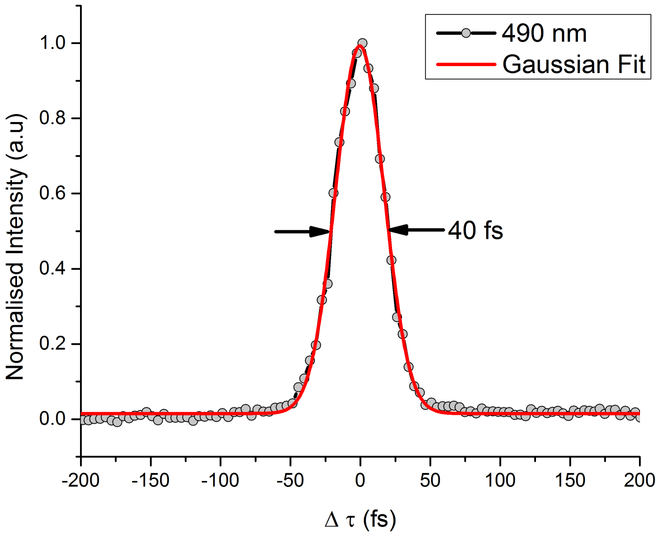

Figure 3.13: An autocorrelation trace as a function of the delay τ between the two incident pulses taken at a wavelength of 490 nm. The FWHM obtained from the gaussian fit is 40 ps.

The pulse envelope $\mathrm{S}(\tau)$ that is measured by the detector is a convolution of the two incident pulses $I_1(t)$ and $I_2(t-\tau)$ (the delayed pulse), and is expressed as

$$\mathrm{S}(\tau) = \int_{-\infty}^{\infty} I_1(t) I_2(t-\tau) dt \tag{3.4}$$

If it is assumed that both input pulses can be described using gaussian profiles, it can be shown that the convolution of the two is also gaussian. Hence, to determine the pulse length, the full-width at half maximum (FWHM) is taken from the measured profile and multiplied by a deconvolution factor of $\frac{1}{\sqrt{2}}$ which originates from Equation 3.4. The FWHM of the autocorrelation pulse shown in Figure 3.13 is determined by fitting a gaussian function. The fit results in a FWHM value of 40 fs and thus, once multiplied with the deconvolution factor, a pulse length of 30 fs is obtained.

4 Analysis of Transient Spectra

4.1 Mercury Dithizonate

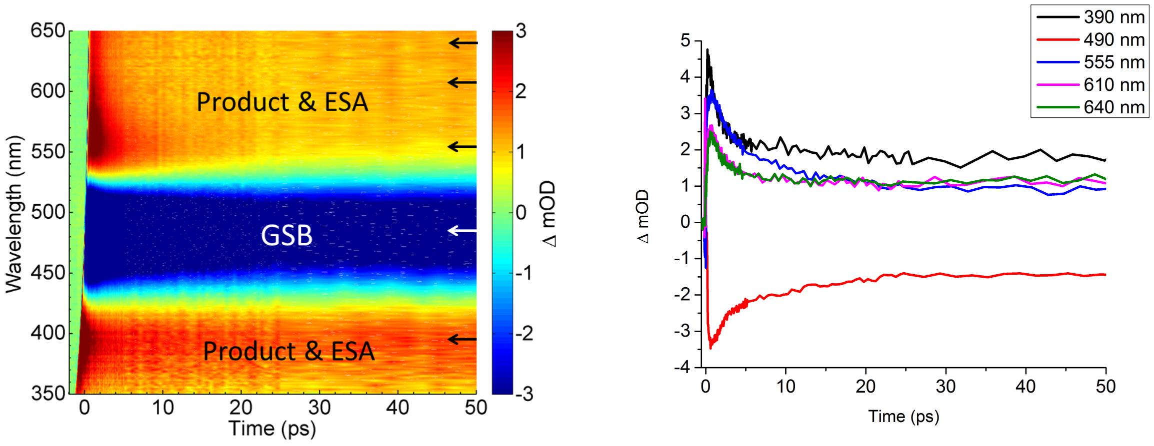

(a) (b)

Figure 4.1: a) Transient absorption spectrum of $Hg(HDz)_2$. b) Temporal lineouts taken at regions of interest from the transient spectrum as indicated by the arrows - note that the GSB signal (490 nm) has been scaled down by a third for clarity.

Mercury dithizonate is the first sample to be analysed as it differs to DPM only by the presence of a second ligand. Figure 4.1a shows the transient absorption spectrum of $Hg(HDz)_2$ obtained when pumped at its steady state absorption maximum of 490 nm. Although data is available up to 500 ps, only the first 50 ps are shown here as the colormap shows no significant changes thereafter. This spectrum has not been corrected for chirp - correcting the chirp in this instance causes an aberration of the signals due to the different time steps available at differing wavelengths. Due to the striking visual similarity between the signals in the transient spectra of $Hg(HDz)_2$ and DPM in Figure 3.1a, the discussion on the origin of the signals mainly follows the analysis of DPM's spectrum in Section 3.1. Despite signals from the same states being visible in Hg(HDz)'s spectrum, there are two points of contention that arises when the temporal lineouts (Figure 4.1b) are considered.

1. In the lineouts depicted in Figure 4.1b, an additional longer time constant, which was not reported for DPM, can be seen. The lineout at 555 nm, in particular, supports this when compared to the other positive decaying signals at 390, 610 and 640 nm. As an estimation of the longer component, bi-exponential fits on the lineouts in Figure 4.1b indicate that it decays at ≈10-12 ps. There is also evidence of this longer component in the GSB signal, which suggests that the ground state may be being repopulated via an additional path or there is spectral overlap. Based on this, there is reason to speculate as to the existence of an additional state which feeds the ground state and primarily shows absorption at 555 nm.

2. After the dynamics that occur in the lineout at 390 nm, the signal remains at a baseline value of roughly 2 ΔmOD. This is significant when compared to the constant value of

Stellenbosch University https://scholar.sun.ac.za

$\sim$ 1 ΔmOD reached by the signal at 610 nm which is known to be due to product absorption. Given that the steady state measurements in Figure 2.1 only show minor product absorption (the blue curve 'directly after illumination' in 2.1) at 390 nm, the product's signal in the transient at 390 nm should be considerably smaller in comparison to what is seen at 610 nm. If one was to assume that the signal at 390 nm is only due to product absorption and the difference in absorption at 610 nm is simply due to a difference in oscillator strengths, the absorption value of the product in Figure 2.1 at 390 nm should be roughly twice the value at 610 nm. As this is not the case, it points to the possibility of a state which decays on a time scale greater than 500 ps, thus effectively contributing a constant value to the spectrum at 390 nm.

To validate the claim that was made with regards to the longer time component mentioned in 1) above, and the possibility of a second transition state, the point of departure for the analysis is the GSB signal. The reason for analysing the GSB first is that under ideal circumstances the population of the ground state is exclusively monitored by this signal. However, in this case, as shown by the non-instantaneous appearance of the GSB signal in Figure 4.2a, there is an overlap with a positive signal. Based on the amplitude of the lineout at 390 nm, the time scale in which the overlap occurs and its profile, one can speculate that the signal that is most likely to contribute is a fast decaying positive signal such as the decay of the instantaneously excited state R* in Figure 3.1b. This is illustrated further in Figure 4.2b where the sum of an instantaneous bleaching signal (green curve) and instantaneous mono-exponential 'fast' decaying excited state (black curve) is shown. The resultant overlap of the two signals shown by the red curve resembles the profile seen in the experimental data in Figure 4.2a. Thus if the recovery of the bleaching signal is monitored roughly from its minimum, the contribution from the shortly lived positive signal should be negligible. Note that it is possible that signals from other states overlap with the GSB at longer times, but in order for the analysis to continue, it is assumed that their contributions are not significant.

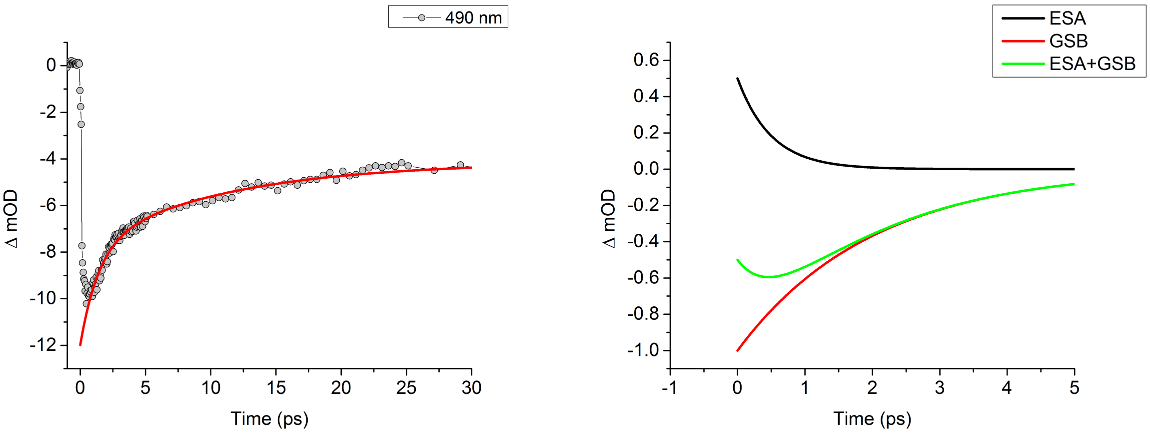

(a) (b)

Figure 4.2: a) GSB signal at 490 nm fitted with a bi-exponential function with averaged rates of 1.4 and 10 ps. b) An illustration of overlap between a instantaneous bleaching signal and a mono-exponential decaying excited state absorption signal.

To obtain an accurate estimation of the time constants associated with the recovery of the ground state bleach, a bi-exponential function is fitted to lineouts (averaged over 5 nm) every

Stellenbosch University https://scholar.sun.ac.za

10 nm from 460 nm to 510 nm[1]. From these fits, recovery rates with averages of 1.4 ps and 10 ps were obtained. In Figure 4.2 the GSB signal is shown with a fit using the averaged rate constants. A recovery of roughly two-thirds of the total signal can be seen. The third that remains absent is mainly attributed to the formation of the product, although there may be processes (such as intersystem crossing) that repopulate the ground state on a longer time scale which are not observed in the available temporal domain.

As the 1.4 ps component of $\mathrm{Hg(HDz)_2}$ is essentially the same as the component reported for DPM it is reasonable at this point to assume that this component plays the same role as in DPM ($\mathrm{k_2}$ in 3.1b) and that DPM's model is transferable to $\mathrm{Hg(HDz)_2}$ (see discussion in 2.2.1). For the $\mathrm{Hg(HDz)_2}$ model this implies that a transition state, $\mathrm{TS_1}$, is included to feed the ground and product state. To account for the 10 ps component an additional transition state, $\mathrm{TS_2}$ is introduced which repopulates the ground state. At this point, the manner in which the two transitions states are populated need to be accounted for. To keep the model pragmatic it is assumed that both $\mathrm{TS_1}$ and $\mathrm{TS_2}$ are populated by the same state, namely, the instantaneously excited state of the reactant form ($\mathrm{R^*}$). A summary of the states involved in the model is given in Figure 4.3, where the decay rates of the different states are given by $\mathrm{k_1}$, $\mathrm{k_2}$, $\mathrm{k_3}$ and $\mathrm{k_4}$. The set of coupled differential equations used to describe the population of each state in the model are given as follows:

$$
\begin{aligned}
\frac{d\mathrm{R}^*}{dt} &= -(k_1 + k_3)\mathrm{R}^* \\
\frac{d\mathrm{TS}_1}{dt} &= k_1\mathrm{R}^* - 2k_2\mathrm{TS}_1 \\
\frac{d\mathrm{TS}_2}{dt} &= k_3\mathrm{R}^* - k_4\mathrm{TS}_2 \\
\frac{d\mathrm{P}}{dt} &= k_2\mathrm{TS}_1 \\
\frac{d\mathrm{R}}{dt} &= k_2\mathrm{TS}_1 + k_4\mathrm{TS}_2
\end{aligned}
$$

The boundary conditions used in solving the differential equations restricted the initial population of $\mathrm{R^*}$ at t=0 to one and the population of all other states to zero. In a model, such as the one above, where a given population decays throughout various states, the amplitude of each state is typically determined by the initial population as well as the rate constants coupling the states. However, in the transient absorption data, the amplitude of the concentration profile of each state is not just dependent on the total number of molecules excited and the rate constants, but also the oscillator strength of the state's transition. If the cross section is known for a given transition scaling can be done accordingly, however, in this case, they are not known. The concentration profiles obtained by solving the equations above are thus multiplied by a scaling parameter to remedy this. In doing so the amplitudes of the concentration profiles obtained in fitting the transient absorption data are of little use and instead, the focus is turned to the rate constants.

---

[1] Attempts to fit the bleaching signal with a single exponential were unsuccessful

Stellenbosch University https://scholar.sun.ac.za

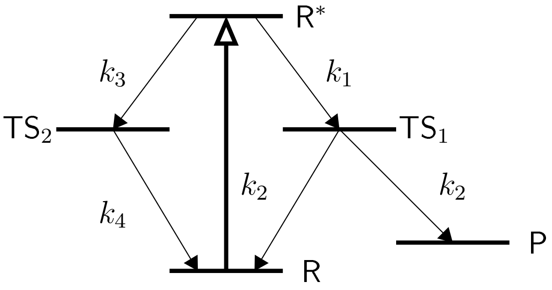

Figure 4.3: Postulated model after fitting the GSB. States are indicated as follows: TS - Transition state, R - Reactant and P - Product. Rates of (1.4 ps)$^{-1}$ and (10 ps)$^{-1}$ were assigned to k_2 and k_4 respectively, after analysis of the GSB.

To test the model, the sum of a combination of the states' population profiles are fitted to the data. Above 550 nm the profiles of both transition states and the product state are included. For the band at 390 nm, the profile of R* is included along with the previously mentioned states. With regards to the parameters, k_2 and k_4 were fixed at rates of (1.4 ps)$^{-1}$ and (10 ps)$^{-1}$ respectively, leaving the scaling parameters of each of the concentration profiles along with k_1 and k_3 to be determined. Initial fits on 'test' lineouts, albeit generally fitting the data well, showed overparameterisation with k_1 and k_3 typically converging to the same value or giving nonsensical values. To resolve this, the two rates were set equal and the fits repeated. With this constraint applied, fits were done in intervals of 10 nm at ranges between 550-640 nm and 370-390 nm and an average value for k_1 and k_3 of (0.5 ps)$^{-1}$ was obtained. Examples of the fits using these values are shown in Figure 4.4 along with their respective residuals. The population profiles of each contributing state is also shown. The lineouts displayed here were chosen to display the fit quality where the signals of the different states are thought to be most prominent: TS$_1$, P and R* at 390 nm and TS$_2$ at 555 nm. It must be noted that the product profile at 390 is assumed to contain a contribution from the long-lived state mentioned in 2). The amplitudes of each scaling factor obtain in the fitting process from 540-640 nm are shown in Figure 4.5 and reveals the absorption profiles of TS$_1$, TS$_2$ and the product in this region. Commentary on these profiles are reserved for the global target analysis in the next section (Section 4.2) where similar profiles should be obtained.

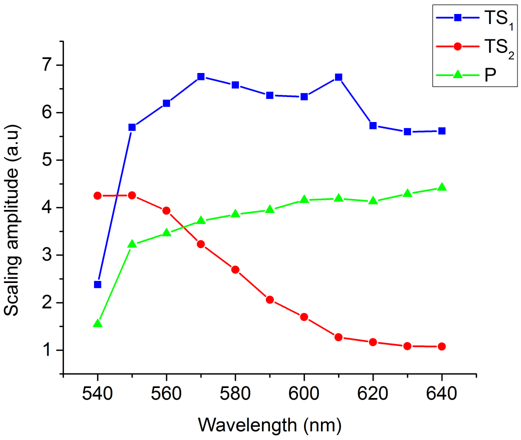

Figure 4.5: Scaling amplitudes obtained for each state's population profile between 540-640 nm.

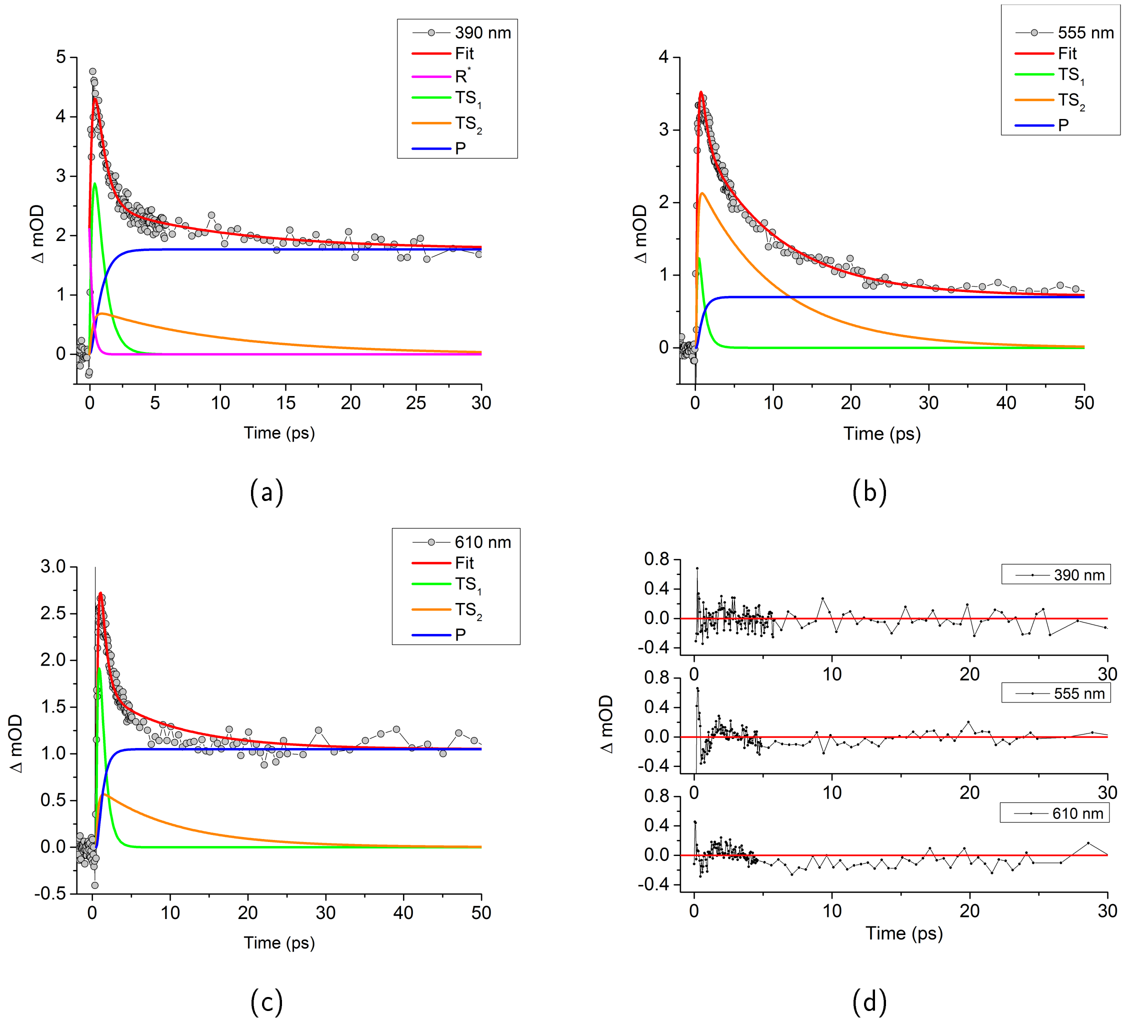

(a)

(b)

(c)

(d)

Figure 4.4: a), b) and c): Fits of temporal lineouts at 390, 555 and 610 nm using the concentration profiles of selected states in the model. d) Residuals of each of fit (i.e the difference between the data and fitted curves).

As an indication of the success of the fits, the residuals are shown in Figure 4.4d. At 390 nm the residuals are generally situated around zero, where as at 555 nm and 610 nm, a more prominent structure can be seen below 5 ps. At 610 nm there is also some mismatch between the data and the fitted model in the interval of 5-15 ps. At this point there are three comments to be made in light of the residual structure: 1) the rate constants found in the ground state are not descriptive of the data globally, 2) the combination of fitted population profiles are not correct, or 3) the model is not suited to the data. Investigating these possibilities further is suited to a global analysis approach where optimal rate constants can be found for the entire dataset. Having become acquainted with the behaviour present in the data will assist with determining whether the unfamiliar global analysis software is being applied correctly to the data.

Stellenbosch University https://scholar.sun.ac.za

4.2 Global Analysis of Transient Spectra

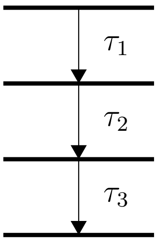

Figure 4.6

The simultaneous global fitting of a transient absorption dataset is known as 'global analysis' or 'global target analysis' if the fitting is constrained by a unique model based on certain hypotheses or assumptions. In order to perform a global fit, two assumptions need to be made [43]. The first is that the data is assumed to be homogeneous, in other words, the system under investigation can be described using a discrete set of parameters. The second is that the data is assumed to be separable. This means that the temporal and spectral evolution contained in the dataset can be separated and thus described by the superposition of different contributing components. Under these assumptions, the data matrix D containing $\Delta OD(t, \lambda)$ can be described using 'i' compartments/states as

$$D(t, \lambda) = \sum_{i=1}^{n} c_i(t) A_i(\lambda) \tag{4.1}$$

where $c_i(t)$ is the convolution of the time-dependent concentration profile (or population profile) of the i^{th} state and the instrument response function (IRF)[2], and $A_i(\lambda)$ is the wavelength dependent amplitude of the i^{th} component's concentration profile [43]. Depending on the concentration profiles used, the interpretation of $A_i(\lambda)$ differs. There are three cases to consider.

1. In the case where the concentration profiles take on the form of independent monoexponential decays (a parallel decaying scheme), the resulting amplitudes contained in $A_i(\lambda)$ are referred to as decay-associated difference spectra (DADS). If the system being considered is composed only of parallel decaying components, the DADS give the spectral profile of each specie. If not, they depict a weighted sum of the species's spectra. These are useful to obtain an idea of the dynamics that take place by considering their profiles as well as whether they are positive or negative. A positive value indicates that ΔOD is decreasing - thus either a positive signal decaying or a negative signal decreasing. Conversely, a negative DADS value indicates that ΔOD is increasing and implies that there is a positive signal increasing or a negative signal increasing. Physically, the positive and negative values are hence translated as follows: DADS<0: bleach or stimulated emission decay, or rising absorption; DADS>0: rising bleach or stimulated emission, or decaying absorption [44].

2. If the model is unknown, the concentration profiles can be modelled using a sequential decay scheme (as shown in Figure 4.6) with increasing lifetimes ($\tau_1 < \tau_2 < \tau_3 < \cdots$). The resulting spectral profiles $A_i(\lambda)$ are then referred to as evolution-associated difference spectra (EADS). The EADS are useful as they allow the evolution of the spectrum to be visualised using the global time constants - the first EADS represents the spectrum at time zero and decays with τ_1, the second EADS rises with τ_1 and decays with τ_2 and so forth [43]. Given that the actual dynamics that occur may differ from a sequential scheme, the individual EADS would display a mixtures of the different compartments/states present in the system. In the case that the system's dynamics are described by a sequential model, $A_i(\lambda)$ represents the species-associated difference spectra (SADS) (see next).

3. If the model for the system being studied is known and the concentration profiles of the states are used in Equation 4.1, the definition of $A_i(\lambda)$ is altered. $A_i^{SADS}(\lambda)$ in this

---

[2] IRF: The convolution of the shape of the laser pulse with the detector's response.

Stellenbosch University https://scholar.sun.ac.za

instance is given, as per definition, by $\epsilon_i(\lambda) - \epsilon_0(\lambda)$ where $\epsilon_i(\lambda)$ is the species-associated difference spectra (SADS) of each state/compartment and $\epsilon_0(\lambda)$ the spectrum of the ground state bleach[3] [43]. The SADS thus represent the spectrum of each state in the postulated model with the ground state bleach subtracted. Ascertaining whether the correct model has been applied is done by looking for abnormalities in the profiles of the SADS, and comparing them to the EADS and DADS. Abnormalities in this case refers to the SADS taking on incorrect values - e.g if it is known that an excited state decays in a certain region and its SADS amplitude is negative.

For data exploration (without a known model), the profiles of the EADS and DADS are examined concurrently. This is critical for our data as we expect a combination of parallel and sequential decays based on the prior analysis. The EADS are typically more convenient and intuitive to use as they show how the spectrum evolves temporally (these are essentially spectral lineouts coupled to the respective decay times), and gives an indication of which states are present at certain times [44]. It must be stressed again that although a sequential model is used to generate the EADS, the model must not be take literally and is used only for explorative purposes. To obtain an indication of the profiles present in each EADS, the DADS are consulted. This is done because the i^{th} EADS is a linear combination of the i^{th} and succeeding DADS. The DADS will thus compliment the interpretation of the EADS as they show the loss/gain of absorption associated with a particular rate and therefore the distribution of each time constant throughout the data. To illustrate how the EADS and DADS are used in data exploration, an analysis is performed on Hg(HDz)$_2$.

4.2.1 Global analysis of Hg(HDz)$_2$

The analysis of Hg(HDz)$_2$ reveals global time constants of 0.3, 1 and 9 ps, and a non-decaying component. To determine whether the fitting was successful, singular value decomposition is performed on the residual matrix and the resulting left (temporal) and right (spectral) singular vectors are consulted (See appendix A.3 for details regarding singular value decomposition). Simply put, these singular vectors contain the temporal and spectral structures/behaviour that reside in the residual matrix. Consequently, a successful fit implies that there should be little to no structure left in either of the singular vectors. The first two temporal and spectral singular vectors of the residual matrix can be seen in Figure 4.7d. The lack of structure in the temporal residuals, apart from the contribution of the coherent artefact, reveals that the dynamics within the data is accounted for with the given number of rate constants. At longer wavelengths the artefact behaves more erratically giving rise to the structure seen in the bottom frame of 4.7d. In this spectral region the artefact typically has two oscillations and the fitting procedure does not always manage to fit both. Regardless, this does not have a significant impact on the analysis and should only influence the accuracy of the shortest time constant.

The EADS and DADS are shown in Figures 4.7a and 4.7b where the evolution of the EADS are given as: EADS 1 $\xrightarrow{0.3ps}$ EADS 2 $\xrightarrow{1ps}$ EADS 3 $\xrightarrow{9ps}$ EADS 4 $\xrightarrow{>>ns}$. EADS 1 represents the spectrum at time zero and displays IESA features below 450 nm and above 530, and a GSB signal which is not initially at its minimum. The IESA features can be attributed to the R* state in our model. The GSB signal only reaches it's minimum in EADS 2 after 0.3 ps - looking at the 0.3 ps DADS suggests that this is due to overlap with the absorption of the IES as the GSB reaches its minimum once this signal has decayed. In the evolution to EADS 2, we see an increase of ESA below 420 nm and above 530 nm. The large difference in amplitudes

---

[3] The terms 'state' and 'compartment' are used here interchangeably.

between EADS 1 and 2, as well as a spectral shift of the peaks, indicates that different states have been populated. EADS 3 shows a substantial decrease of the ESA below 420 nm and above 530 nm as well as recovery of the GSB signal. Lastly, EADS 3 → EADS 4 shows a prominent loss of ESA at 550 nm and GSB recovery. The loss of absorption at 400 nm is less pronounced. EADS 4, which is non-decaying on this time scale, primarily shows long-lived absorption at 400 nm and above 530 nm as well as a persisting bleach signal.

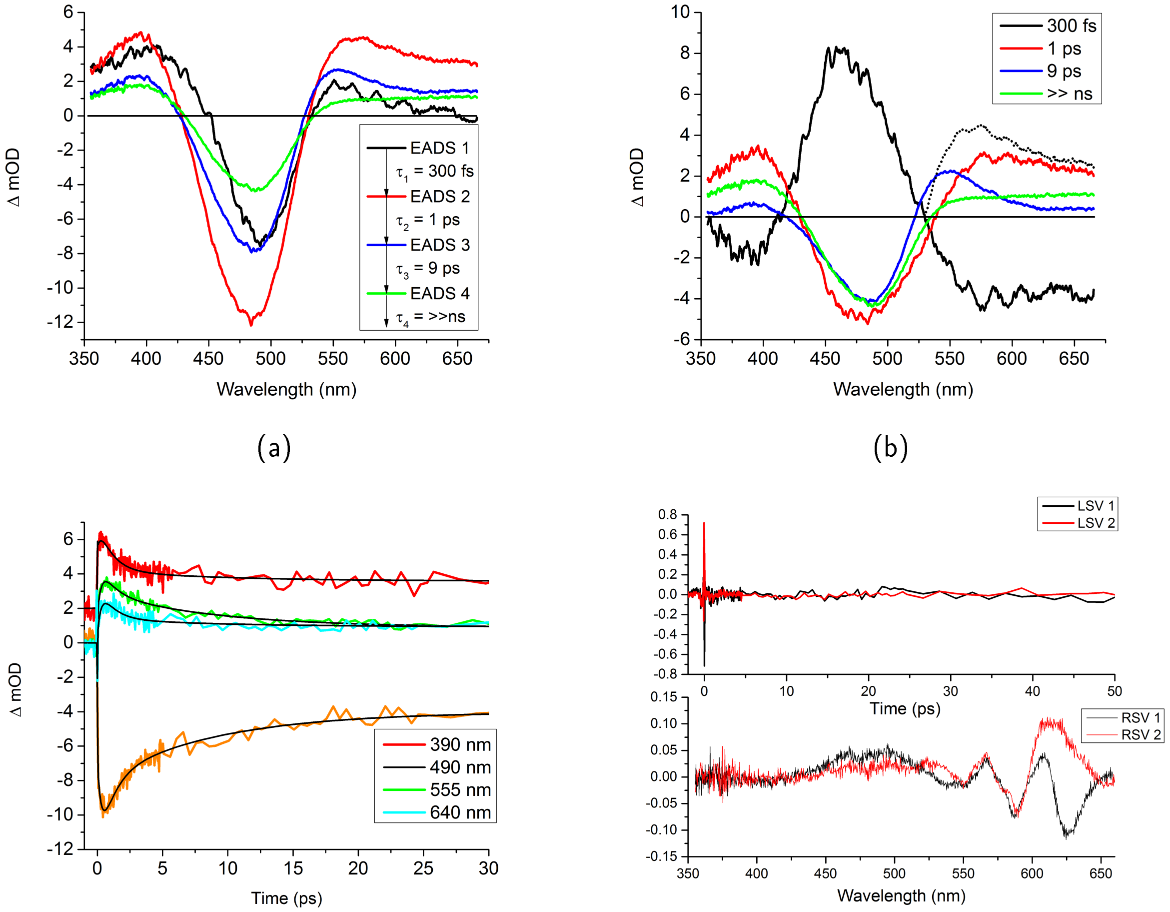

(a) (b)

(c) (d)

Figure 4.7: a) and b): EADS and DADS of Hg(HDz)$_2$ respectively. All curves were smoothed for clarity. c) Fits of selected lineouts. The curve for 390 nm is vertically offset. d) First two left (temporal) and right (spectral) singular vectors of the residual matrix as an indication of the fit quality.

Evidence of two transition states

By comparing EADS 2 and EADS 3 (along with the 1 and 9 ps DADS) the profile above 530 nm suggests that two spectrally overlapping states may be present: one predominantly showing absorption which peaks at 550 nm and decays at 9 ps, and the other a broader absorption above 550 nm decaying at 1 ps. To illustrate this further, the dotted profile in Figure 4.7b is obtained when adding the 1 and 9 ps DADS above 530 nm, and closely resembles EADS 2. Furthermore, the dotted profile resembles a mirror image of the 0.3 ps DADS, indicating that these states should both rise with 0.3 ps. In light of our model this means that EADS 2 contains a contribution from TS$_1$ and TS$_2$ and EADS 3 primarily from TS$_2$. These two states also show absorption below 430 nm, but the similarity of the profiles in this region allow no further comments to be made. The flat absorption profile above 620 nm present in EADS 3

Stellenbosch University https://scholar.sun.ac.za

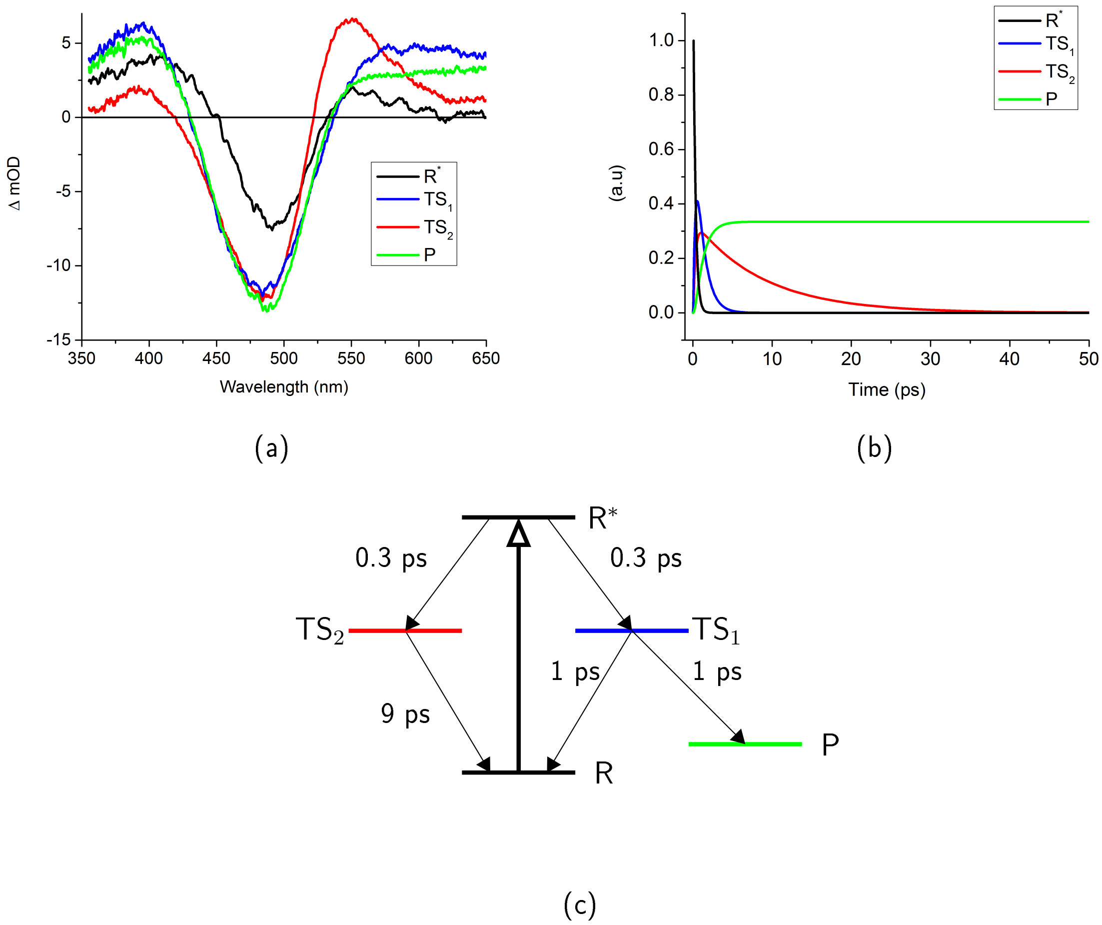

(a)

(b)

(c)

Figure 4.8: Target analysis of Hg(HDz)$_2$. a) SADS obtained in target analysis. b) Colour coded concentration profiles of the respective SADS. c) Model used in target analysis with the determined time constants.

is associated with the product absorption. The slight vertical offset between EADS 3 and 4 in this region is a result of the noise in the data or would otherwise indicate that the product, or part thereof decays at 9 ps. The latter is not in accordance with what is expected.

GSB behaviour

Concerning the general behaviour that takes place at the GSB signal at 490 nm, the red and blue DADS show that the ground state recovers at two rates. By the evolution of EADS 2 → EADS 3 → EADS 4 one can see that the bleach recovers two-thirds of its initial bleaching amplitude. Of the two-thirds that is recovered, a third is recovered at a rate of 1 ps and the other third at 9 ps (these fractions are determined by comparing the amplitude of EADS 2 and 3 to the non-decaying EADS at 490 nm). Seeing as the DADS and EADS above 530 nm suggest the presence of two states which decay at 1 and 9 ps, there are grounds to believe that both these states should empty into the ground state.

Target analysis

In light of the global analysis results revealing similar dynamics to those obtained in the prior analysis, the model that was postulated in Figure 4.3 is used in the global target analysis. The SADS, along with their respective concentration profiles, are shown in Figures 4.8a and 4.8b, and the model with the global time constants in Figure 4.8c. With regards to the SADS, commentary on their profiles is limited as the electronic structure of the molecule is

Stellenbosch University https://scholar.sun.ac.za

not known[4]. We note that the profiles of each state above 530 nm appear to match those obtained in the earlier analysis. The profiles which raise some suspicion are those of TS_2 and the product. The flat TS_2 profile above 620 nm indicates that a contribution from the product absorption may still be present. The product profile is not in accordance with the expected profile of the product's spectrum in Figure 2.1 which peaks at 610 nm. It must be noted that provisions for other long-lived states have not been made in the model, and the product SADS would thus contain contributions from them accordingly. Again, as in the prior analysis, the 400 nm region shows a product SADS amplitude roughly double that of the amplitude above 550 nm which suggests this may be true (as argued in point (2) in Section 4.1). As for the region above 550 nm, assuming that the contribution from long lived states is negligible here, the flat SADS profile points to the possibility of shorter lived product isomers which broaden the absorption. Sertova *et al.* showed that continuous illumination of $Hg(HDz)_2$ (dissolved in chloroform) at three different wavelengths between 436 - 550 nm resulted in steady state product absorption bands with different absorption maxima between 580-600 nm. As our data was only collected at one pump wavelength and on a completely different time scale to that of Sertova *et al.* we are unable to comment directly on this. Although a white light source was used for excitation in Figure 2.1, we do not see evidence for product isomers. Since they were only visible under continuous irradiation in Sertova *et al*'s measurements, it must be assumed that they decayed prior to taking the measurement shown in Figure 2.1 and hence only the main long lived product is seen. Separating possible isomer profiles in a TAS measurement would be possible if transient spectra at different pump wavelengths were collected. Doing this may also reveal whether different dynamics are observed when the excitation energy is varied and whether the rate at which the isomers form is affected.

Analysis summary of $Hg(HDz)_2$

In comparison to the analysis method followed earlier (Section 4.1), the global analysis yielded similar results, with the time constants only differing slightly. The target analysis provides further confirmation that the postulated model is capable of describing the dynamics present in the data. The difference in residuals between the prior analysis and this analysis is attributed mainly to the slight difference between the time constants. The SADS indicate that the location of the states in the prior analysis were correct - the only difference being the presence of the R^* absorption around 550 nm. The analysis of $Hg(HDz)_2$ has shown that upon photo-excitation there are two reaction paths through TS_1 and TS_2 back to the ground state. As was found for DPM, the pathway through TS_1 is associated with the formation of the orthogonal intermediate that results in product formation or repopulation of the ground state. At this point commentary on the second reaction pathway cannot be made. As this pathway was not reported for DPM it is possible that the second ligand in $Hg(HDz)_2$ is responsible for this. The ligand is consequently discussed next as we will be able to isolate single ligand dynamics to which we can compare our analysis of $Hg(HDz)_2$.

Comments on Global analysis

The global analysis routine, has the benefit of providing additional spectral information in the form of EADS, DADS and SADS as well as global time-constants that describe the dataset in its entirety. This makes deciphering and identifying the dynamics across the dataset more efficient. Furthermore, features such as the coherent artefact and IRF which were not considered in the prior analysis, can also be accounted for in the software. Pre-processing of the data is also streamlined as Glotaran offers features such as background correction, SVD analysis, averaging etc. that streamlines tasks that would otherwise have to be done by hand. There is also no need to correct the chirp in the dataset as this is included in the analysis regime. The analysis

---

[4] This holds for all the samples that are discussed

of the remaining samples is consequently done using Glotaran.

4.3 H_2Dz: The ligand

The 9 ps associated with TS_2 in $Hg(HDz)_2$, which has yet to be assigned to a physical process, prompts an investigation of the dynamics of the ligand prior to considering the remaining metal dithizonates. This will elucidate any differences that may occur due to the ligand being complexed with a metal or the presence of a second ligand. The presence of similar dynamics, especially a component in the vicinity of $\approx$9 ps, in the ligand can thus be used to rule out any involvement of the second ligand. The dynamics of the ligand are only considered when pumped at 610 nm as this is exclusive to the π-conjugated keto form of the ligand. Pumping at the other 450 nm absorption maxima will result in an excitation of both the keto and non-conjugated enol form. Furthermore, as the ligand retains its π-conjugated system in the ligand, the dynamics that take place should be better represented by exciting the keto form[5].

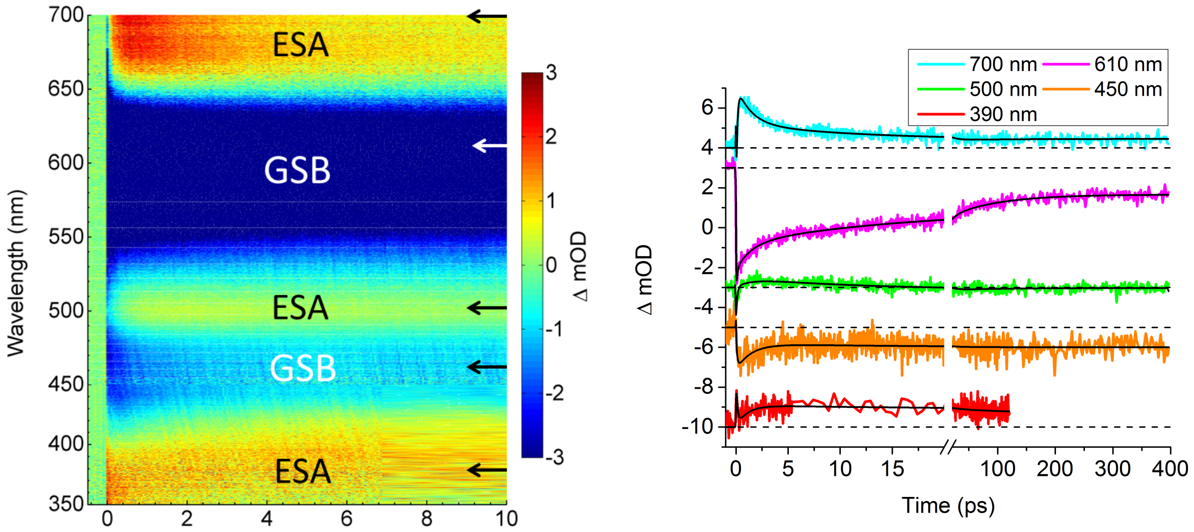

(a)

(b)

Figure 4.9: a) Transient absorption spectrum of H_2Dz obtained at a pump wavelength of 610 nm. The two spectral regions made accessible for probing by CaF_2 and Sapphire crystals have been stitched together in this figure. b) Temporal lineouts corresponding to the arrows in a). The 610 nm lineout has been scaled down by a half. The black curves indicate the fits obtained using global analysis. The 390 nm lineout was taken from a measurement using the CaF_2 supercontinuum which had a smaller temporal domain.

The transient spectrum of dithizone in Figure 4.9 features five distinct signals when pumped at 610 nm: three excited state absorption signals at 380 nm, 500 nm and 680 nm, and two bleaching signals at 470 nm and 600 nm. Global analysis reveals four time constants of 140 fs, 1.3 ps, 12.4ps and 85 ps, and a non-decaying component[6]. The ultra-short component of 140 fs

---

[5] Despite this, a measurement at the NOPA's lower signal limit (470 nm) was performed and the results shown in Appendix A.4. The dynamics are not discussed further as they appear to differ considerably to those that will be discussed

[6] To double check these values, manual fits were also done and similar rates obtained

Stellenbosch University https://scholar.sun.ac.za

is not considered accurate as it falls within our temporal resolution limit and is also distorted by the coherent artefact. It was however necessary to include this contribution to avoid significant structure in the temporal residuals. The residuals are shown in Figure 4.10c. The EADS and DADS associated with these rates are shown in Figures 4.10a and 4.10b. For clarity, the region of each signal in the transient spectrum is marked in the background of the aforementioned figures. Note that the global analysis was run separately on measurements taken using the supercontinuum generated by CaF_2 and Sapphire crystals, and the resulting DADS and SADS were joined together. Despite obtaining similar time constants, the amplitudes differed and caused the vertical offset visible in the EADS and DADS at 450 nm.

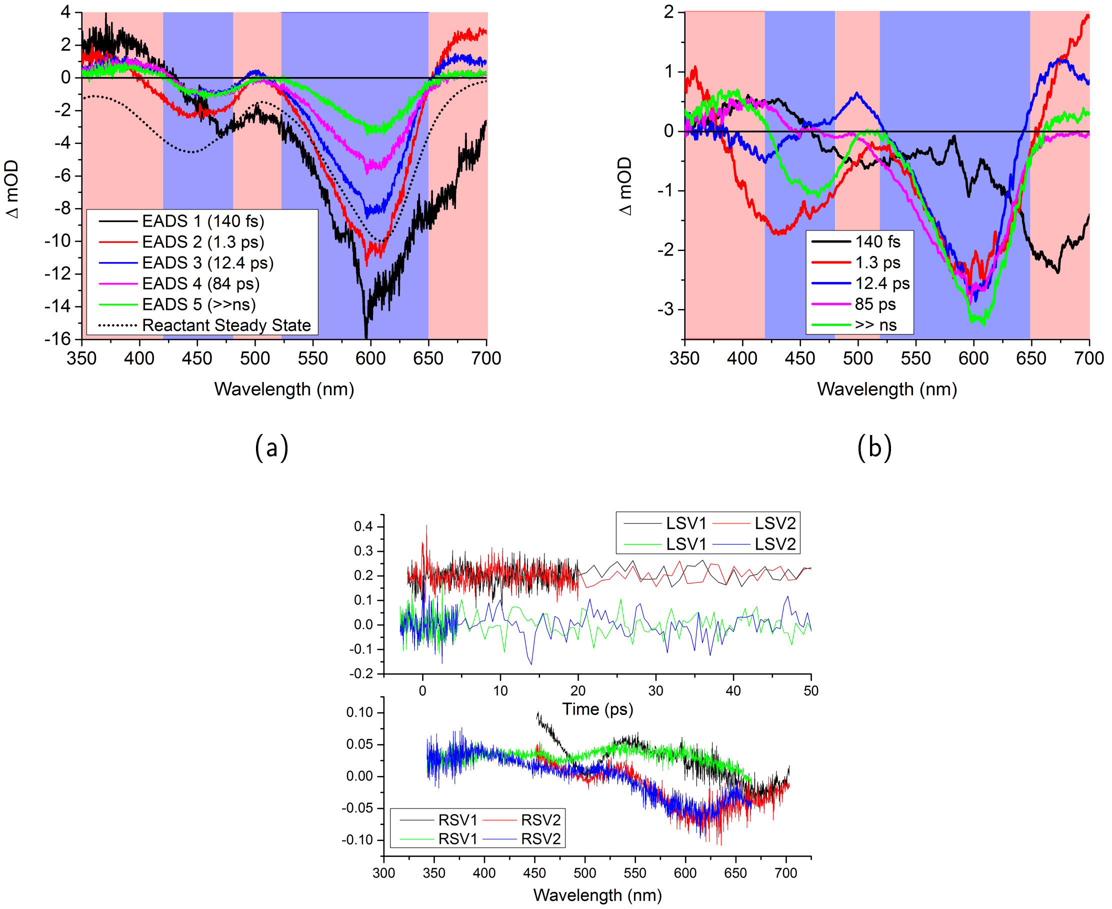

(a)

(b)

(c)

Figure 4.10: a) and b): Smoothed EADS and DADS resulting from global analysis. The 140 fs DADS has been scaled by a quarter for clarity. The steady state profile in the EADS (dotted curve) has been inverted and scaled down. c) Temporal and spectral singular vectors of the residual matrix. Black and red pertain to the measurement using Sapphire; Green and blue to the measurement using CaF_2.

Bleaching signals

The analysis of the ligand's transient spectrum starts with the GSB signal at 610 nm as the most revealing dynamics occur here. The time zero EADS spectrum (black curve) which includes GSB/SE decays quickly in 140 fs. The procession of the EADS at 610 nm that follow indicate that the ground state recovers 70% of its initial bleach amplitude with three rates (1.3, 12.4 and 85 ps) with the remaining 30% residing in the product state (and possibly

Stellenbosch University https://scholar.sun.ac.za

another long lived state). The 1.3 ps and 85 ps components each contribute roughly 20% to the ground state recovery whilst the 12.4 ps component contributes slightly more at 30%. The signal at 450 nm is also due to ground state bleaching as pumping the molecule at 450 nm causes the bleaching signal at 610 nm to appear instantaneously (See Appendix A.4). In this case however, the 450 nm bleaching signal is caused by a transition from the ground state R to a energetically higher lying reactant state R$_m$ where as the signal at 610 nm is to a lower lying state R$_n$. A summary of the transitions are given in Figure 4.11. We would thus expect to see the bleaching at 450 nm also recover with three rates, but this is not the case. This bleaching signal only shows a recovery with a single rate of 1.3 ps. The fact that the other two rates are not directly visible here (the 12.4 and 85 ps DADS are zero here and the EADS show no temporal changes) is likely the result of the weak noisy signal and the two positive competing signals on either side.

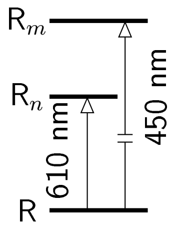

Figure 4.11

Transition states

The three-component-recovery of the GSB suggests three different reaction paths that lead to the the ground state. The 1.3 and 12.4 ps rates suggest that similar transition state reaction paths (TS$_1$ and TS$_2$ respectively) to those found in Hg(HDz)$_2$ should be assigned. The EADS and DADS above 650 nm, using the same arguments followed for assigning transition states in Hg(HDz)$_2$, appear to support this: i.e EADS 1 appears to contain a contribution from both the 1.3 and 12.4 ps DADS. At this point, we maintain that the model as postulated should remain unaltered. This leaves the 84 ps decay component into the ground state unaccounted for. Judging by the similar shape of the negative 12.4 ps DADS and positive 85 ps DADS between 375-450 nm, the 85 ps decaying state should rise at a rate of 12.4 ps. Consequently an additional transition state (TS$_3$) is included which branches off TS$_2$ and leads to the ground state: TS$_2$ $\xrightarrow{12.4ps}$ TS$_3$ $\xrightarrow{85ps}$ R. It must be noted that the ESA band below 400 nm is very noisy due to the low amplitude of the white light in this region (see Figure 3.6) and therefore the assignment is not necessarily trustworthy. A summary of the model which has been adjusted to include this path is shown in Figure 4.12.

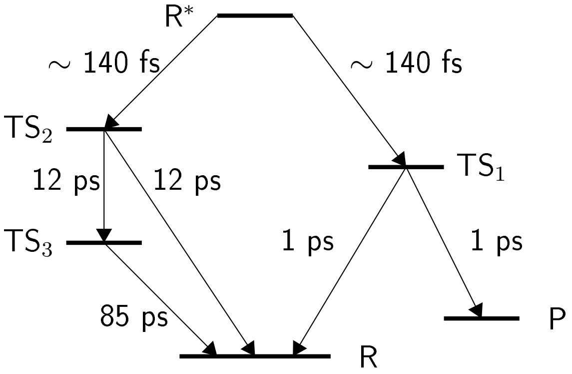

Figure 4.12: Postulated model for H$_2$Dz. The model for Hg(HDz)$_2$ was adapted to include a third transition state that branches from TS$_2$ and feeds into the ground state.

Ambiguities regarding TS$_2$ and the product

In assigning the reaction scheme as depicted in Figure 4.12 the peak at 500 nm in the EADS and DADS leads to speculation with regards to 1) the rise time of TS$_2$ and 2) product formation.

Stellenbosch University https://scholar.sun.ac.za

1. The delay in the appearance of the ESA signal at 500 nm, which can be seen in the transient spectrum and the EADS, may suggest that a rise time of 1.3 ps should be more appropriate for TS_2. We can however also argue in favour of a shorter rise time if this delay is caused by the overlap of a weakening bleach signal - initially the signal at 500 nm indicates that bleaching is present here (considering the profile of the steady state reactant absorption this is not unexpected). If this is the case we should expect to see the bleaching signal return once T_2 has decayed. The 500 nm lineout in Figure 4.9b suggests that this is not the case, however, it must be noted that the signal here is small and relatively noisy; other lineouts in this vicinity indicate a long lived bleach whilst others indicate ESA. It may be that the bleaching signal here is simply too weak to observe once TS_2 has decayed. Alternatively one could speculate whether there is another long lived state which absorbs in this region, but this would imply that its absorption cancels that of the bleach exactly - an unlikely scenario. The weak signal in this region makes it difficult to determine which of these scenarios is taking place.

2. The long lived absorption present below 425 nm and above 650 nm in EADS 5 is assumed to be due to the product formation. In assigning the decay path through TS_1 we have implicitly implied that its absorption is too weak to be noticeable in the third EADS. Based on our model and the product formation in $Hg(HDz)_2$ we maintain that this should be the case. However, the formation and profile of the product poses a conundrum when the results from Grummt *et al.* are considered [19]. Due to the different solvents, timescales, excitation energies and solution concentrations used, the results presented here in DCM are not necessarily directly comparable to those obtained by Grummt in hexane/acetone (recall that the ligand is salvato- and concentrato-chromic). Despite this, their observation of a millisecond-decaying product band at 520 nm in their flash irradiation study of the ligand allows for further speculation on the results presented here. In our measurements there is no visual evidence of long-lived product formation (up to 400 ps) in the aforementioned region[7]. It is possible that the short-lived state at 500 nm which we have assigned as TS_2 may thus represent the decay of a secondary unstable product form. The consequent formation of TS_3 from TS_2 would thus have to relate to a state occupied in the secondary unstable product form (TS_2) or the formation of a tertiary unstable product form. Our lack of knowledge of the product limits further discussion on the matter. A continuous irradiation study in DCM where the ligand is excited at both wavelengths independently should provide the necessary information to investigate this matter further.

The ambiguities mentioned above are a clear indication that further investigation is required to resolve the dynamics of the ligand in detail. This is beyond the scope of this study. The most important information to take away from the analysis is that the ground state is repopulated at rates of 1.3 ps and 12.4 ps, similarly to what was found for $Hg(HDz)_2$. Although a 85 ps component is also present, it is of little interest to our interpretation. More importantly, we have shown that the 1 and 12 ps components are intrinsic to the ligand. This rules out any possibility that the $\approx$10 ps component through the secondary reaction pathway observed in $Hg(HDz)_2$ could be associated with the presence of a second ligand. We can thus expect $Zn(HDz)_2$ and $Pb(HDz)_2$ to display similar, if not the same, reaction pathways and dynamics.

Target analysis

Despite the uncertainties pertaining to TS_2 and the product, the postulated decay scheme shown in Figure 4.12 was used in the target analysis. The SADS are shown in Figure 4.13a

---

[7] It must be noted that at the other pump wavelength of 470 nm this was also the case (see Appendix A.4)

Stellenbosch University https://scholar.sun.ac.za

along with their associated concentration profiles in Figure 4.13b. There are no significant abnormal features in the spectra, although the profile of the TS_1 profile below 450 nm is questionable as the bleach does not extend this far. This is due to the data from measurements using different crystals to generate the probe beam being stitched together (this can also be seen in the 1.3 ps DADS). It is interesting to note that the broad profile of TS_1 and peaked profile of TS_2 above 650 nm bears resemblance to those obtained in $Hg(HDz)_2$ above 530 nm (See Figure 4.8a). Comparatively speaking, the metal does not seem to influence these two reaction paths since the rate constants are very similar, but there is a difference in the wavelengths at which these 'paths' are visible. The steady state spectra in Figure 2.4 indicate that the absorption maximum of the ligand is shifted 120-80 nm when a metal is added. This shift is similar to that of TS_1 and TS_2 when comparing the ligand and $Hg(HDz)_2$.

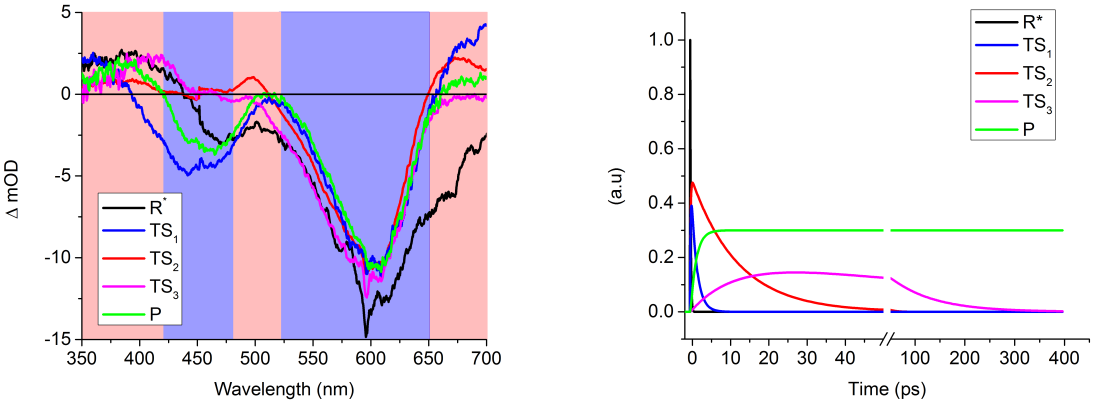

(a) (b)

Figure 4.13: a) SADS obtained in target analysis. b) Respective colour-coded population profiles for each SADS.

4.4 Zinc Dithizonate

If the claim about the ligand's intrinsic dynamics holds, we expect two reaction pathways through TS_1 and TS_2 with rates of $\approx$ 1 and $\approx$ 9-12 ps to be present in $Zn(HDz)_2$ and $Pb(HDz)_2$. This was indeed the case for $Pb(HDz)_2$: the analysis (see appendix A.1) displayed similar rate constants (0.9 and 10 ps) through the two reaction pathways, as well as very similar excited state absorption profiles in comparison to $Hg(HDz)_2$. Due to the similarity to $Hg(HDz)_2$ there is no need to discuss the matter further. $Zn(HDz)_2$, on the other hand, will be considered in more detail as there are noticeable differences which prompts further investigation.

Stellenbosch University https://scholar.sun.ac.za

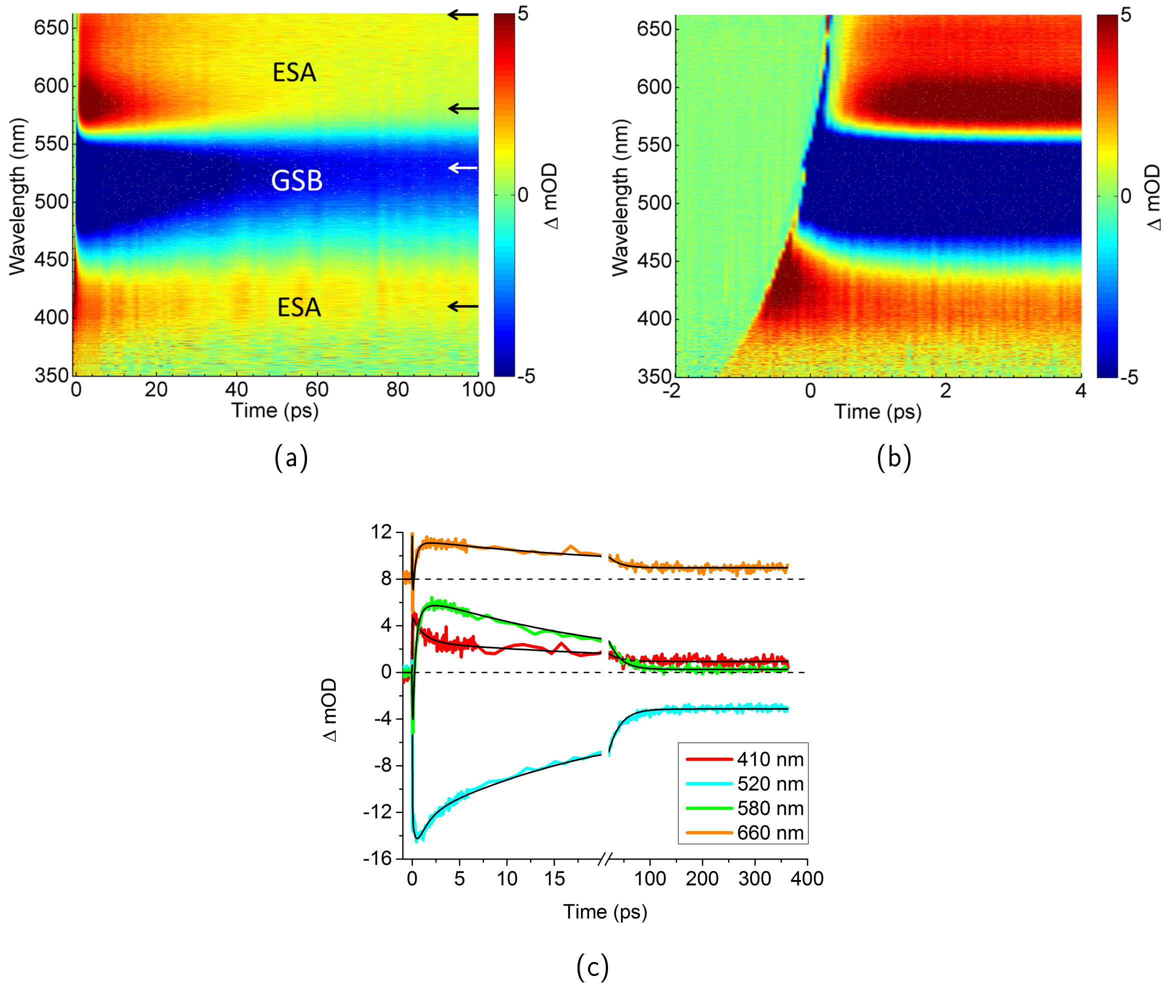

(a)

(b)

(c)

Figure 4.14: a) and b): Transient spectra of $Zn(HDz)_2$ on long and short time scales. Regions of interest are marked with arrows. c) Lineouts at the regions of interest in the transient spectrum along with the fits obtained using global analysis.

The transient spectrum of $Zn(HDz)_2$ in Figure 4.14a closely resembles that of $Hg(HDz)_2$: a bleaching signal surrounded by ESA on both its long and short-wavelength flanks. The prominent differences are a spectrally shifting GSB signal, as well as a SE/GSB signal above 560 nm. The latter is visible more clearly in the transient spectrum in Figure 4.14b. The global analysis required three components with lifetimes of 0.38, 1.2, 23 ps along with a non-decaying component to obtain a suitable fit of the data. The success of the fits are indicated by the fits of the temporal lineouts in Figure 4.14c and lack of structure in the temporal singular vectors in the top frame of Figure 4.15c. The resulting EADS and DADS are shown in Figures 4.15a and 4.15b.

Dynamics of the EADS and DADS

EADS 1 shows IES absorption below 480 nm, GSB at 530 nm and SE above 570 nm. The inverted steady state absorption spectrum of the reactant form shown in the EADS (dotted curve) makes assigning SE to the region above 570 nm easier to see - i.e the bleaching occurs in the spectral region of the steady state absorption and does not extend further than ≈570 nm. $Zn(HDz)_2$ is the only sample that displays SE prior to the appearance of the ESA in this region and was not observed in the transient spectra of $Hg(HDz)_2$ or $Pb(HDz)_2$. The SE originates from the IES to energetically lower lying states. The evolution to EADS 2 (in 1.2

ps) shows the rise of ESA above 560 nm and a blue-shifted absorption below 450 nm. The GSB reaching its minimum in this EADS is attributed the the overlapping IES absorption as shown by the 0.38 ps DADS - this is the same scenario described for Hg(HDz)$_2$ (See 4.2.1. The overlap between the IES and the GSB results in a slight blue shift of the GSB (comparing EADS 2 to EADS 1) once the IES decays. Continuing to EADS 3, there is a further blue shift of the ESA below 400 nm, a decrease in the GSB signal and significant change in profile of the absorption above 550 nm. EADS 4, the non-decaying component, shows the product absorption as well the remaining bleach signal of 20%. Amplitudes of the other EADS in the bleaching region suggest that roughly 24% and 56% is recovered with rates of 1.2 and 22.3 ps respectively.

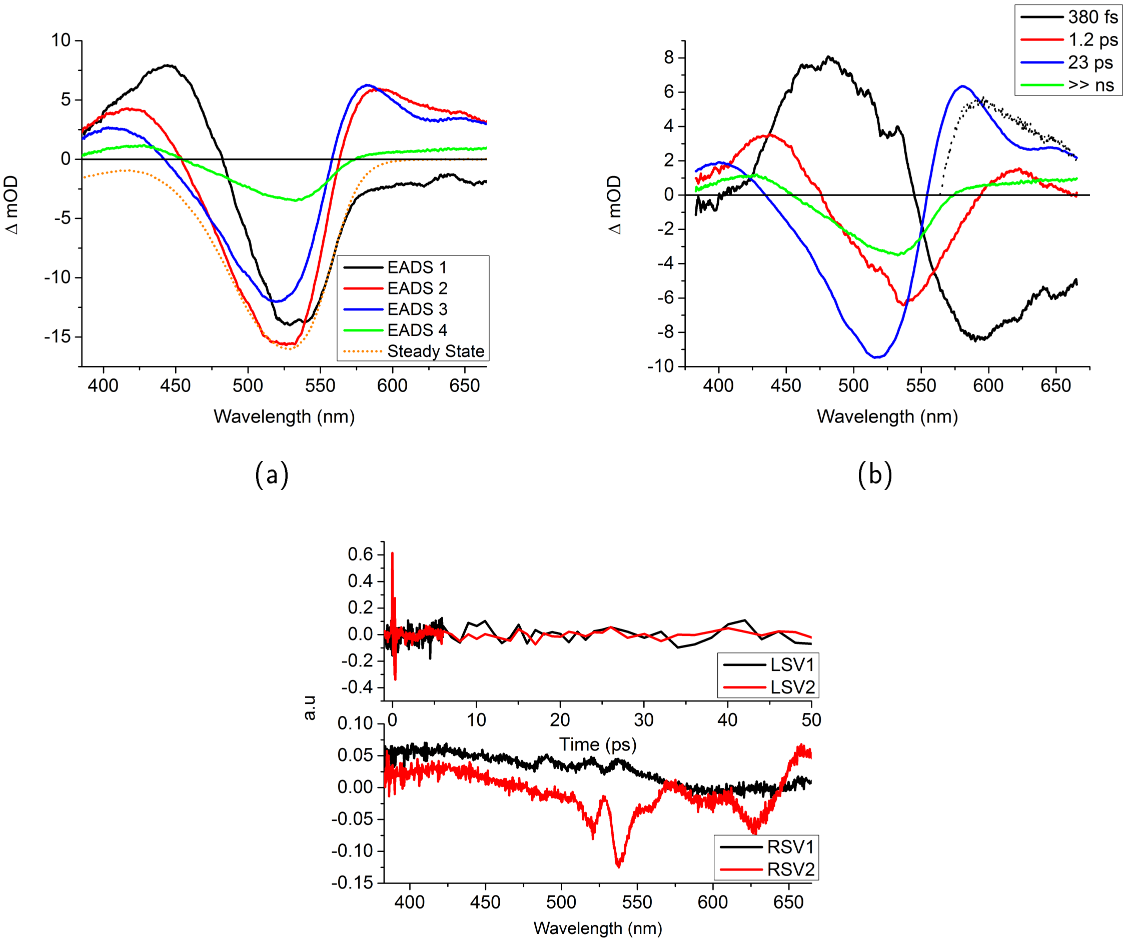

(a) (b)

(c)

Figure 4.15: a) and b) EADS and DADS resulting from global analysis of the transient spectrum. See text for explanation of dotted line in the DADS. The steady state spectrum has been inverted and scaled down in the EADS e) Left (temporal) and right (spectral) singular vectors of the residual matrix.

Transitions states and product formation

Similarly to what was found for Hg(HDz)$_2$, the EADS and DADS above 560 nm again suggests the presence of two transition states. The red and blue DADS are in support of this argument and show two distinct profiles for each TS. Both states appear to be present after 0.38 ps - when adding the 1.2 and 23 ps DADS together (indicated by the dotted line), a profile similar to that of EADS 2 is obtained and it is reminiscent of the mirrored 0.38 ps DADS. In comparison

Stellenbosch University https://scholar.sun.ac.za

to $Hg(HDz)_2$ and $Pb(HDz)_2$ the preliminary profiles of the two transition states (based on the 1.2 and 23 ps DADS above 550 nm) are fairly different, but we retain commentary until the SADS have been obtained. Based on the product yield of 20% and 24% recovery of the GSB at a rate 1.2 ps, we claim that the product should also form at a rate of 1.2 ps. This is derived in accordance with the model as postulated thus far: the bifurcation at the conical intersection (through TS_1) should roughly distribute the excited population equally between the product and ground state with equal rates. The low amplitude of the non-decaying component (green DADS), which is associated with the product absorption, does not allow us to speculate in which EADS above 550 nm it appears. It is known that the product form of $Zn(HDz)_2$ absorbs at 610 nm, and based on $Hg(HDz)_2$, it is reasonable to assume that it should also be present in the ESA band below 450 nm. The only contention with the product forming with a rate of 1.2 ps then is that the difference between the profiles of EADS 3 and 4 below 460 nm suggests that the product appears after the decay of EADS 3 (22.3 ps). If the product does form at 1.2 ps, the profile of the non-decaying component in this region should be visible in EADS 3. This is not the case, but as EADS 3 is negative here (460 nm), it is difficult to say whether there is a contribution from the product. Then again, as with $Hg(HDz)_2$, there is the possibility of a longer lived state that absorbs in this region, and is caught up in the non-decaying spectrum.

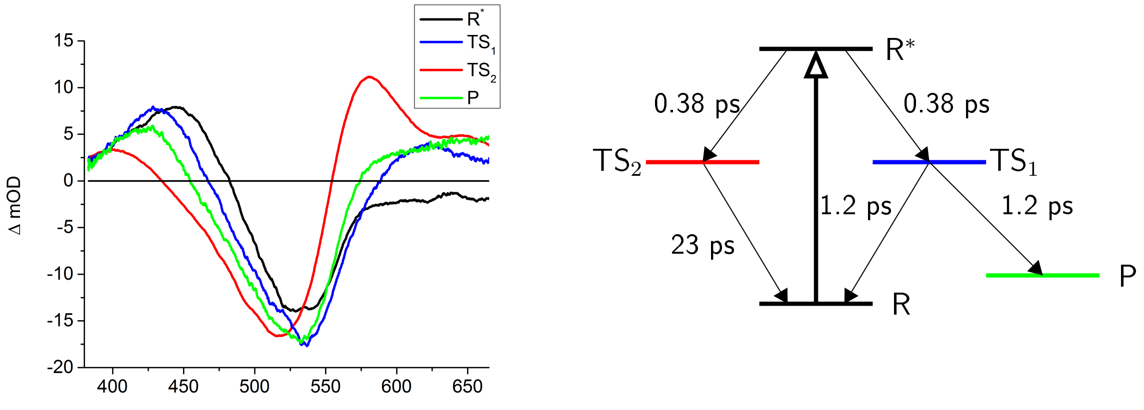

(a)

(b)

Figure 4.16: Target analysis of $Zn(HDz)_2$. a) SADS b) The model used for target analysis and the resulting time constants.

Target Analysis

In keeping with the same model as for $Hg(HDz)_2$, the target analysis yields the SADS shown in Figure 4.16a and the resulting time constants shown in Figure 4.16. The profile of TS_2 is of particular interest as it contains two peaks. The peak at 580 nm next to the GSB is characteristic in all the samples (although the wavelengths differ), but the secondary peak at 640 nm is not. One can debate whether this peak indicates an unresolved state in the analysis, or whether it is a spectral property of TS_2. The R^* state, unlike $Hg(HDz)_2$ and $Pb(HDz)_2$, is negative in the region of 560-650 nm and is attributed to SE. The reason for SE from R^* only being visible in $Zn(HDz)_2$ at these wavelengths is likely due to a difference in oscillator strengths of the transitions. The product absorption, as with $Hg(HDz)_2$ and $Pb(HDz)_2$, has a broad profile above the GSB that increases towards longer wavelengths. Given that the product's absorption peak is situated at ≈610 nm, we again speculate that isomeric product forms may cause the broadened profile [24].

Stellenbosch University https://scholar.sun.ac.za

4.5 Nickel Dithizonate

The transient spectra of nickel dithizonate, shown in Figures 4.17a and 4.17b, displays a vastly different transient spectra in comparison to the metal dithizonates considered thus far. Only the transient spectrum obtained using a pump wavelength of 670 nm is shown here as pumping at the other absorption maxima (470 and 560 nm) showed almost identical spectra (see Appendix A.2 for the spectra obtained using these pump wavelengths.). The dissimilarity of the transient spectra relative to the dithizonates discussed already is expected considering its unique steady state spectrum. What was not necessarily expected is for the transient spectra to contain the same signals regardless of the pump wavelength used: bleaching/SE centered at 670 nm, two distinct ESA regions at 590 and 520 nm and the formation of what appears to be a product at 470 nm. Lineouts taken from the transient spectrum at these regions are shown in Figure 4.17c. A lack of bleaching at 560 and 475 nm when pumping at these wavelengths was noticeable from the spectra at 'low' pump fluences. This must be attributed to IES absorption which overlaps and dominates the bleaching signal.

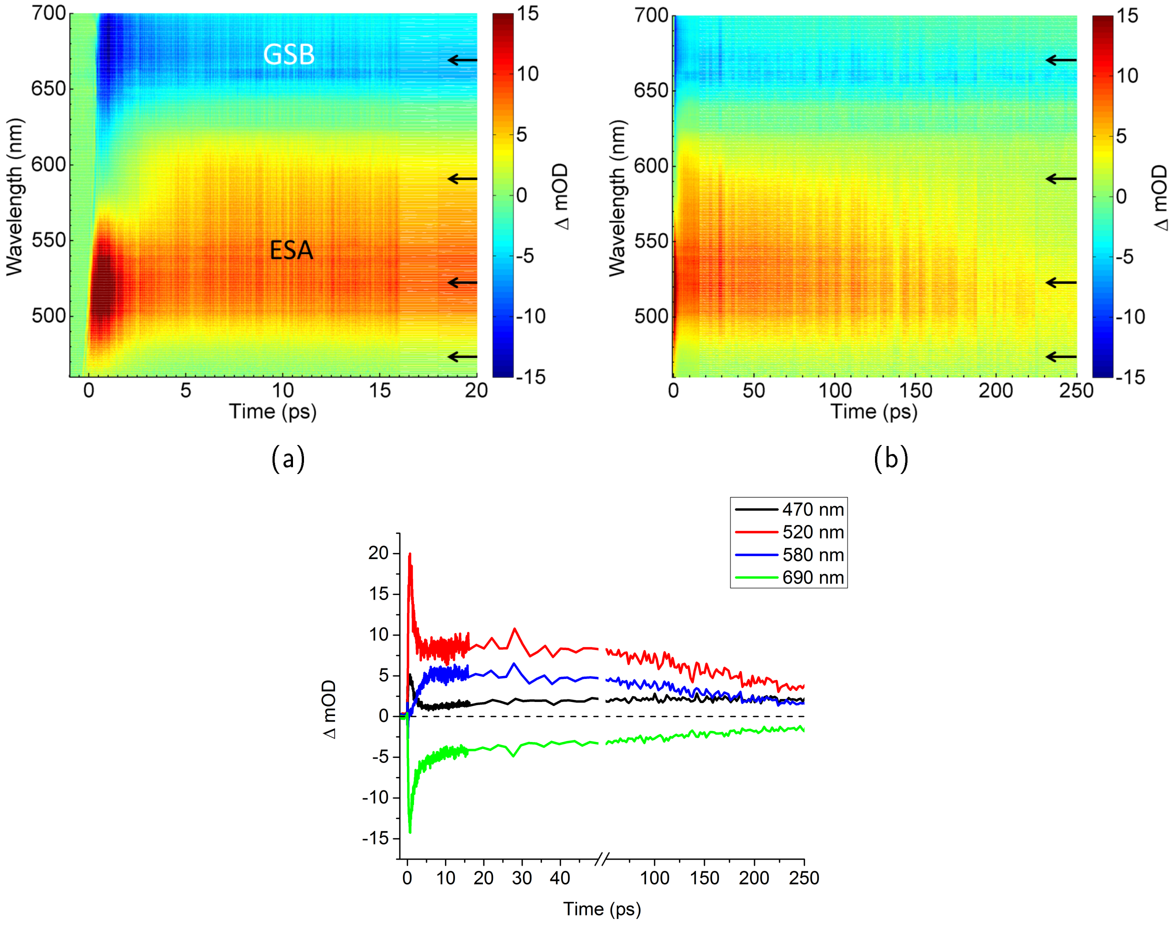

(a) (b)

(c)

Figure 4.17: a) and b) Transient absorption spectra of $Ni(HDz)_2$ on a 'short' and 'long' time scale. This spectrum was obtained at a pump wavelength of 670 nm. Spectra at the other two absorption maxima (470 and 560 nm) are not shown as they are virtually identical. c) Select lineouts at the regions indicated by the arrows in a) and b).

With no prior knowledge of this molecule, except for the possibility of metal to ligand charge

Stellenbosch University https://scholar.sun.ac.za

transfer or ligand-ligand interactions, the interpretation of these signals requires further investigation which is beyond the scope of this study. It must be noted however that initial analysis reveals time constants of ≈0.5, 1, and 10 ps at each pump wavelength, similarly to what was found in the other dithizonates. The fact that these rates are present in Ni(HDz)$_2$ indicate the presence of ligand oriented processes which may be similar to those obtained in the other dithizonates. That being said, 'new' ≈3-5 ps and ≈150-250 ps components were also present when pumped at all wavelengths. A longer component in the region of 300 ps , similar to the 250 ps component in the nickel samples was obtained when the ligand was pumped at 470 nm. Consequently, an analysis on the ligand when pumped at this wavelength can be done in parallel to Ni(HDz)$_2$ to separate ligand specific dynamics. There is also evidence for a non-decaying product component in the region below 530 nm that forms at a rate of ≈ 10 ps. Further commentary is reserved at this stage. Density functional calculations to determine the product form, HOMO and LUMO maps and the origin of the transitions at 475, 560 and 670 nm are currently under way[8] and should provide the required information to unravel the dynamics.

4.6 Summary and interpretation

An overview

In DPM, deactivation after photo-excitation follows a trajectory on the rotational isomerisation coordinate to a single orthogonal transition state which can decay at 1.5 ps via two paths: the one path leads to product formation, and the other, a re-population of the ground state. Under the assumption that this model should hold for Hg(HDz)$_2$, we found that the product formation and ground state recovery occurred with a similar time constant of 1 ps. However, an additional ≈10 ps component in the data was also present, and based on its appearance in the ground state recovery, a second transition state (TS$_2$) was included to account for this. Because a similar component was not reported in DPM, it was uncertain whether the longer component was due to the second ligand in Hg(HDz)$_2$ or was intrinsic to the ligand/molecule. The ligand was thus investigated and revealed the same time constants found in Hg(HDz)$_2$. This suggested that the 1 and 10 ps components are intrinsic to the ligand and that the second ligand in Hg(HDz)$_2$ does not contribute to the dynamics (at least not on a sub-500 ps time scale). Further confirmation of the ligand's intrinsic reaction paths would be provided if Zn(HDz)$_2$ and Pb(HDz)$_2$ showed similar dynamics. This was the case for Pb(HDz)$_2$, but not necessarily for Zn(HDz)$_2$. In the latter, the decay through TS$_2$ is impeded and a decay rate of 23 ps was observed. In totality, the hypothesis in Section 2.2.1 regarding the first isomerisation scheme is thus correct. A summary of the rate constants, percentage of the ground state recovered and product yields are shown in Table 4.1.

The cardinal point to take away from all the analyses, regardless of whether the model accurately reflects the dynamics in all cases, is that we have shown only a single ligand undergoes photo-excitation. If the other ligand does undergo isomerisation in a step-wise manner, it is definitely not reflected in the time scale of our data: the isomerisation of the second ligand would cause a doubling of the product absorption as well as a decrease in the bleaching signal. Neither of these were observed. If it does occur, it must take place at times greater than 500 ps. The appearance of the ≈ 1 ps time constant in all the samples (including Ni(HDz)$_2$ at all pump wavelengths and H$_2$Dz when pumped at 470 nm) indicates that isomerisation should occur in all the samples. That being said, we were unable to obtain well-defined product pro-

---

[8] These calculations are currently being undertaken by our collaborators Prof K. von Eschwege and Prof J. Conradie at the University of the Free State.

Stellenbosch University https://scholar.sun.ac.za

files; the long lived components associated with the product displayed a broad flat absorption. We attributed this to either product isomers or other long lived states which do not decay within the temporal domain available to us.

Table 4.1: Time constants (in ps) and branching ratios obtained for each sample. The rate of product formation is equal to the rate given in column two.

	Rise of TS_1/TS_2 (ps)	Decay constants and their contribution to GSB recovery ps (%)			Product yield (%)
$Hg(HDz)_2$	0.3	1 (33.3)	9 (33.3)	-	33.3
$Zn(HDz)_2$	0.4	1.2 (24)	23 (56)	-	20
$Pb(HDz)_2$	-	0.9 (70)	10 (18)		12
H_2Dz	0.3	1.5(20)	12(30)	84(20)	30

The postulated model

The model that has been used throughout the analysis is shown in Figure 4.18 where it is visualised in terms of singlet potential energy surfaces (PESs). Upon excitation into an unknown higher-energy reactant state, a sub-picosecond radiationless decay leads to two reaction pathways. As it drawn in Figure 4.18, we assume that a conical intersection connects S_n and S_1 which provides the fast radiationless decay. The first path traverses along the isomerisation coordinate similarly to DPM. The second decay path is not observed in DPM and as we have found that this path is intrinsic to the ligand, it is unknown why it was not observed in DPM. Assigning a physical interpretation to this decay route is purely speculative. The only information at hand that may offer an explanation beyond reasonable doubt is that C=N isomerisation can occur via either in-plane inversion or rotation, or a linear combination of both. The short 1 ps component has already been attributed to deactivation along the rotational coordinate. The route along TS_2 may thus be due to a partial evolution on the inversion coordinate which produces an unstable intermediate that decays back to the ground state. In our data there was no reason to suspect that the product forms with the longer time constant (or possibly with both) and thus reinforces the previous statement. To test whether isomerisation via the inversion coordinate is possible, measurements could be performed at increased excitation energies to try and overcome the energy barrier that this path poses. Alternatively, to check whether the isomerisation is strictly rotational, the metal dithizonate could be altered by introducing a functional group or molecule to the N-N-Ph chain that is coupled to the ligand structure and does not allow rotation.

Stellenbosch University https://scholar.sun.ac.za

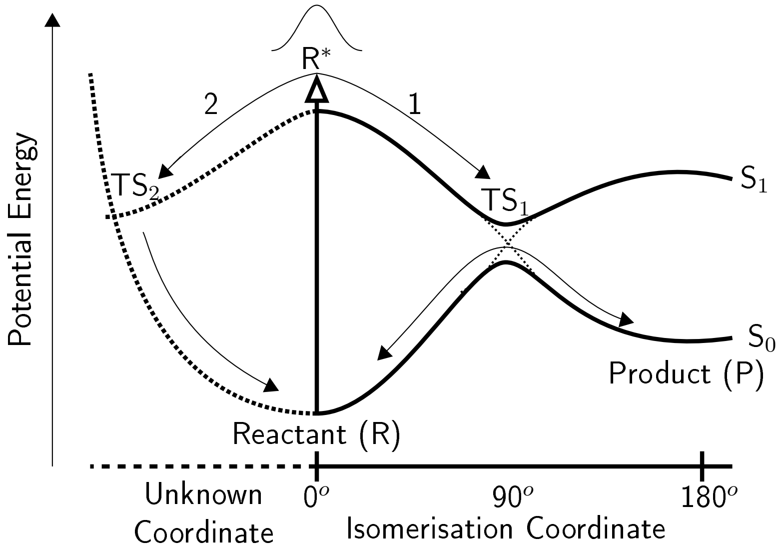

Figure 4.18: The model used in the analysis of the two-liganded metal dithizonates visualised in terms of potential energy surfaces. After the initial excitation, deactivation occurs by means of two paths: '1' and '2'. The first path evolves along the known isomerisation coordinate and the second path on an unknown coordinate. The dotted surfaces are purely hypothetical and are included for illustrative purposes.

The effect of the metal

In the tetrahedral Hg, Zn and Pb complexes, the metal's influence on the steady state spectra is predominantly seen as a shift of the absorption maximum. In our measurements it appears to influence the redistribution of the excited population through the two reaction paths (see Table 4.1. In the case of Zn(HDz)$_2$, the metal's effect is more pronounced, where the decay through TS$_2$ is considerably slower and contributes 56% of the ground-state recovery. We are unable to give a definitive explanation of this, but the reason should reside in the manner in which the metal interacts/distorts the ligand's orbital system. The effect of the metal is also seen in the product yield, although it must also be noted that the product yield was estimated based on the amplitude of the incomplete ground state recovery. Hence, if there are other long-lived states present, our estimation of the product yield may not be accurate. In light of the PESs, the differences in product yield implies that the location of the S$_1$ minimum relative to the S$_0$ maxima changes - i.e if the S$_1$ minimum is located at angles $<90^o$ the reactant is favoured and for angles $>90^o$ the product is favoured.

5 Conclusion

The first ultrafast transient absorption spectroscopy measurements were performed on a group of two-liganded metal dithizonates and the associated ligand. The analysis of $Hg(HDz)_2$ revealed two reaction pathways, of which one was not expected based on prior findings on DPM. The second ligand in the complexes was ruled out as a contributing factor based on similar observations in the ligand. As further confirmation of this, the $Pb(HDz)_2$ and $Zn(HDz)_2$ also showed two reaction paths. The rotational isomerisation pathway yielded a time constant of ≈ 1 ps, similar to DPM. As isomerisation about a C=N bond can occur by means of rotation or inversion, the second pathway was interpreted as a partial evolution on the inversion coordinate where an unstable intermediate is formed which decays back to the ground state. This path was particularly prominent in $Zn(HDz)_2$, but we were unable to give an explanation for why this is the case. Although there may be discrepancies in our model, we have definitively shown that only a single ligand undergoes isomerisation.

The uncertainties in the analyses indicate that there is still an extensive amount of investigation required. In order to distinguish the excited states profiles, measurements can be performed at different probe polarisations (an anisotropic study) and the measurements compared. The different anisotropies of the states should allow them to be separated. Seeing as the ligand displays solvato- and concentrato-chromic properties, solvent and concentration dependent transient absorption studies should also be done. The solvent used is known to alter the ultrafast rates in DPM, but its effect has not been established for other dithizonates [13]. It is reasonable to assume that similar observations are expected. Other effects that are facilitated by different solvents may also come to light. For instance, Sertova *et al.* could not detect product formation when $Hg(HDz)_2$ samples (in DCM) were illuminated with 526 nm light. In chloroform on the other hand, product absorption was detectable. Concentration dependent TAS studies could highlight why the ligand's absorption undergoes changes at higher concentrations [16]. On a merely speculative basis, at higher concentrations intermolecular interactions such as charge transfer processes for example, are likely to become significant. There is also the need to investigate the different dithizonates' more thoroughly from the picosecond to millisecond regime to elucidate the dynamics of the product, product isomers and possible triplet states. Continuous irradiation studies at different wavelengths and solvents can further assist with product related queries in this regard. Further investigations on the product involving a double-pump TAS setup must also be considered to determine whether the product is also photo-active. One study has claimed that this was observed when $Hg(HDz)_2$ was embedded in a polymer, however, there have been no other reports (to our knowledge) which have replicated these results in an aqueous environment [9]. With regards to the planar dithizonates such as $Ni(HDz)_2$, they can be considered separately from the tetrahedral complexes ($Hg(HDz)_2$, $Zn(HDz)_2$ and $Pb(HDz)_2$) investigated in this study. The likely involvement of both ligands and the metal in the photo-reaction makes analysing the dynamics from a purely spectroscopic point of view difficult.

The metal dithizonates in general offer opportunities to investigate various fundamental processes in physics and chemistry. Our results have shed some light on the dynamics that occur in these molecules, but have also highlighted various areas that need to be addressed and that there is an extensive amount of research to be undertaken in order to fully grasp their behaviour.

Stellenbosch University https://scholar.sun.ac.za

Appendices

Stellenbosch University https://scholar.sun.ac.za

A Further information on TAS measurements

A.1 Lead Dithizonate

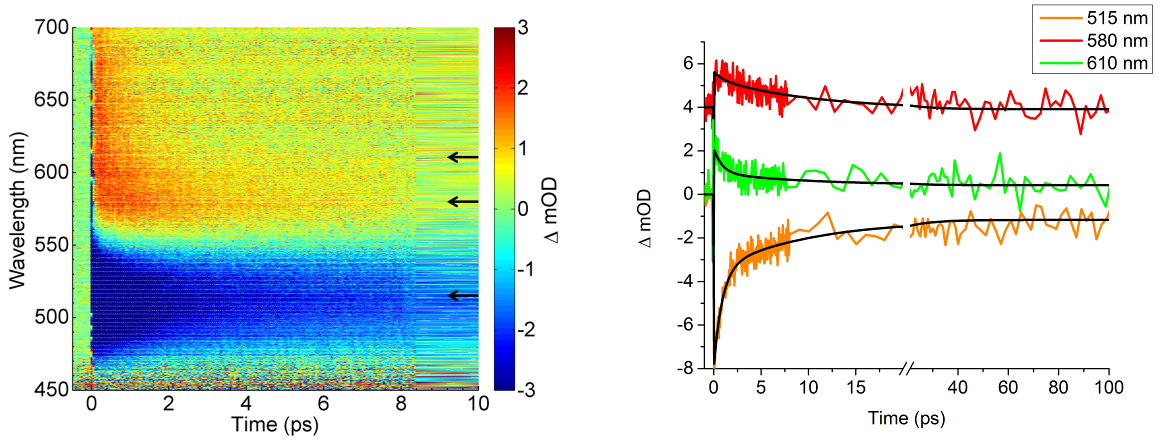

(a)

(b)

Figure A.1: a) Transient absorption spectrum of $Pb(HDz)_2$. b) Lineouts at selected regions indicated by the arrows in a)

The transient spectrum shown in Figure A.1a is similar to that of $Hg(HDz)_2$. In this case the spectral range is limited by the supercontinuum generated in Sapphire (≈450-700 nm). The measurement obtained in CaF_2 was discarded due to excessive noise, but it did show an ESA band below 450 nm which is characteristic to the two-liganded dithizonate samples. Due to the similarity of the $Pb(HDz)_2$ EADS and DADS (shown in Figures A.2a and A.2b) to those obtained in $Hg(HDz)_2$ see the discussion in Section 4.2.1 for further explanation.

Stellenbosch University https://scholar.sun.ac.za

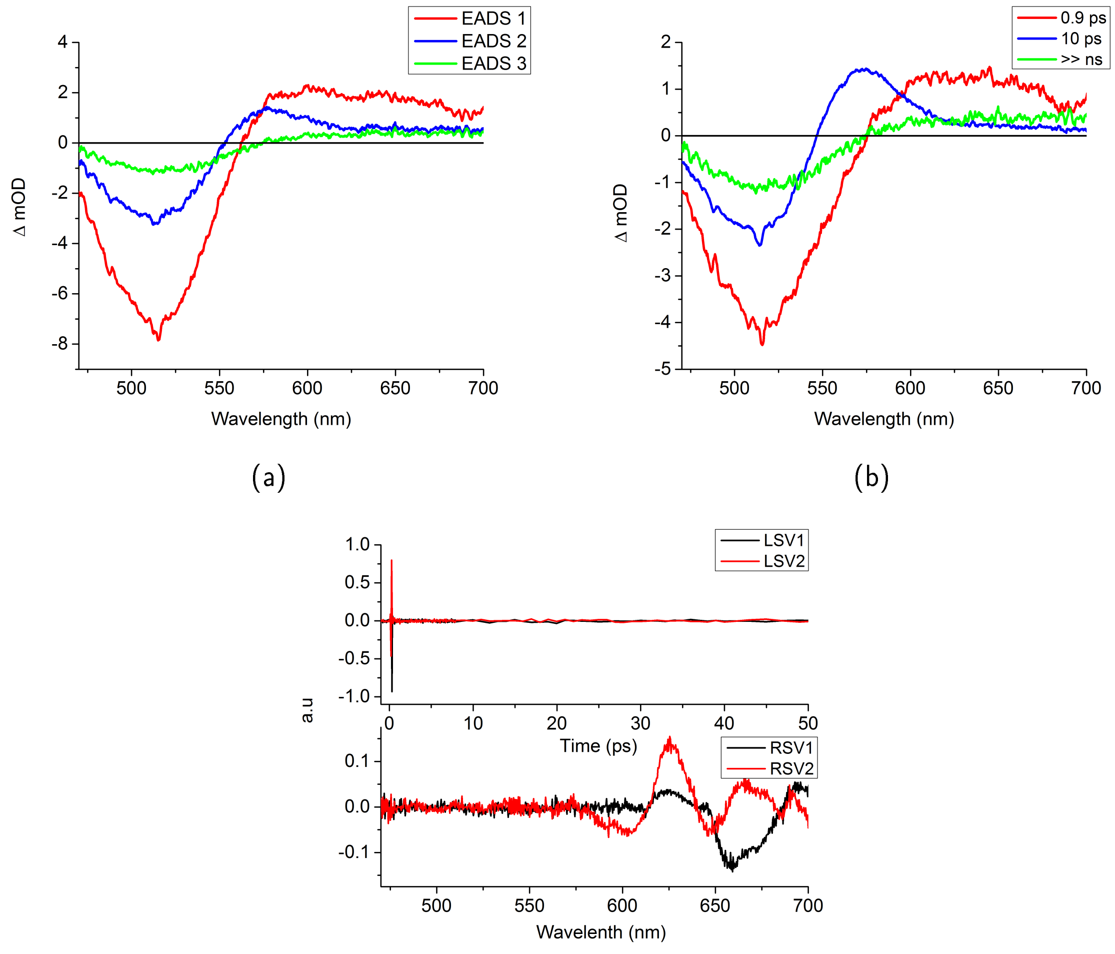

(a) (b)

(c)

Figure A.2: Global analysis of Pb(HDz)$_2$. a) and b): EADS and DADS. These are comparable to the EADS and DADS obtained in the analysis of Hg(HDz)$_2$ (see Figures 4.7a and 4.7b) c) Left (temporal) and right (spectral) singular vectors of the residual matrix.

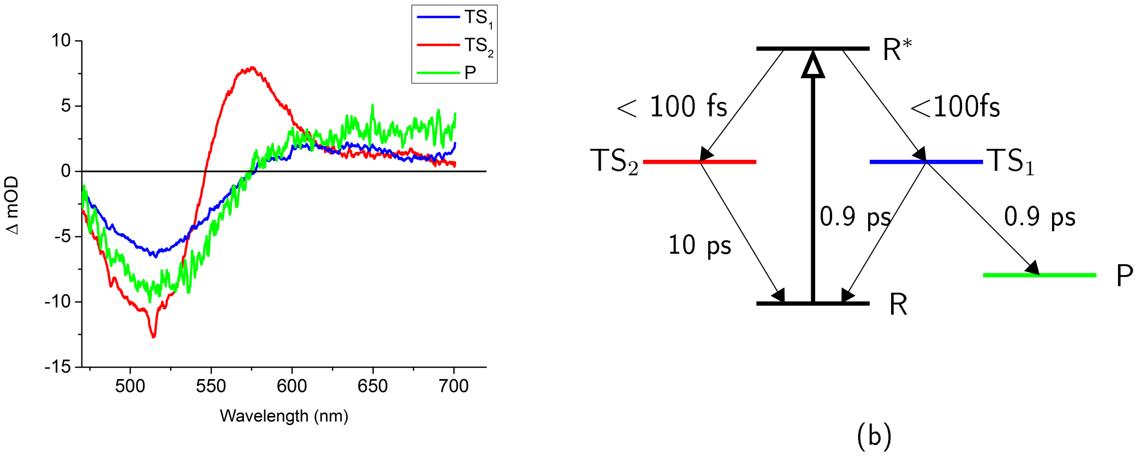

(a) (b)

Figure A.3: Target analysis of Pb(HDz)$_2$. a) SADS obtained using target analysis. b) Model used in target analysis.

Stellenbosch University https://scholar.sun.ac.za

A.2 Nickel Dithizonate

The transient spectra obtained at pump wavelengths of 475 and 560 nm are shown in Figures A.4a and A.4c. At 560 nm the pumping region was removed due to excessive scattering and the information in this region consequently lost - subtracting the scattering only resulted in a distortion of the signal due to the high pump fluence used to obtain a significant signal to noise ratio[1]. The same holds for when the sample was pumped at 475 nm.

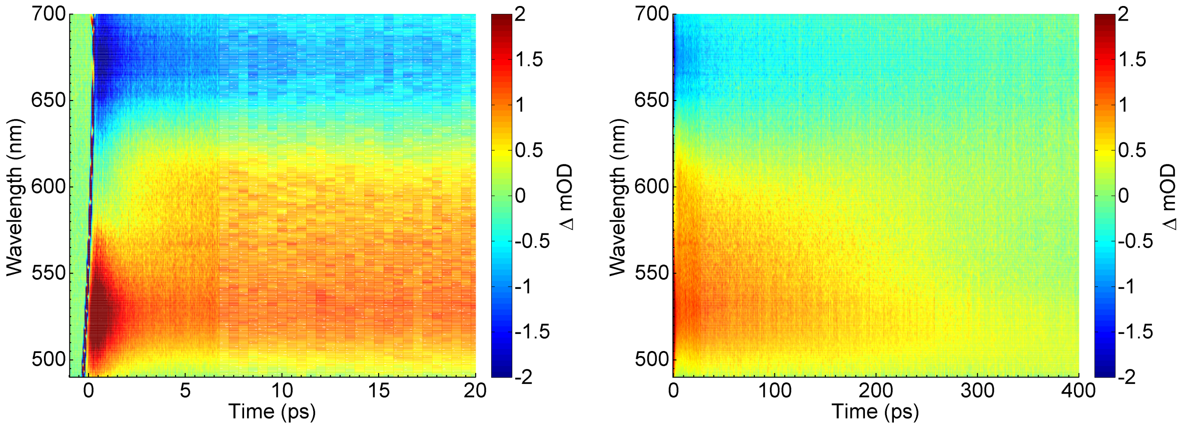

(a) Pumped at 475 nm

(b) Pumped at 470 nm

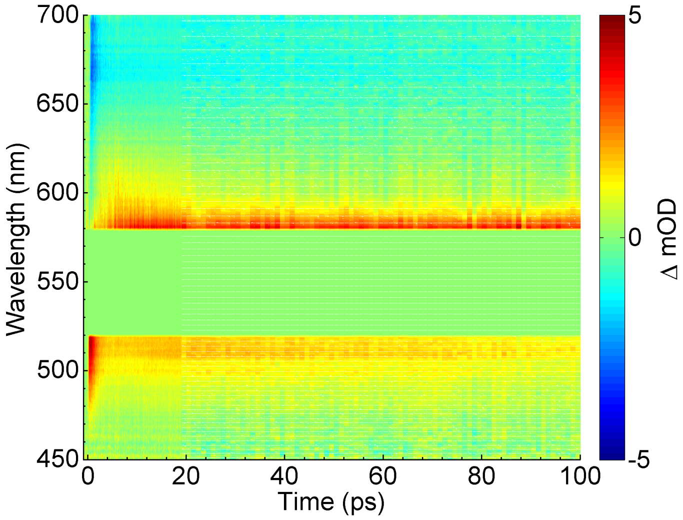

(c) Pumped at 560 nm

Figure A.4: a) and b) Transient absorption spectra of Ni(HDz)$_2$ when pumped at 475 nm. c) Transient absorption spectra of Ni(HDz)$_2$ when pumped at 560 nm. The pumping region at 560 nm has been removed due to excessive scattering.

A.3 Singular value decomposition

The purpose of performing singular value decomposition (SVD) on a TAS dataset is to decompose the data matrix D such that it can be represented by n components that reflect the most prominent contributions to the data. The columns of the experimental data matrix contains

---

[1] Measurement performed at decreased pump fluences also showed no bleaching signals at these wavelengths

Stellenbosch University https://scholar.sun.ac.za

the temporal data and the rows, the spectral data. If we were to perform SVD on the matrix D(t, λ), we would have that

$$D = USV^T \tag{A.1}$$

where the columns of U and V contains temporal transients (left singular vectors) and spectra (right singular vectors) respectively, and S contains the n singular values in decreasing order along the diagonal. The singular values can be seen as weighting factors. Each singular value, along with its associated temporal and spectral profile, gives a particular 'behaviour' present in the data. As the singular values are in decreasing order in S, it allows for the most prominent contributions to the data to be found. This is useful in the initial analysis of the data to give an indication of the number of kinetics/compartments. An example of this is shown in Figure A.5. Performing SVD on the residual matrix of a resulting fit can thus show whether there is still behaviour/structure remaining that has been unaccounted for. This was used extensively in judging the quality of the fits. Although this has not been used in out analysis, SVD can also be used to 'simplify' the experimental data by reconstructing it using only the most prominent singular vectors.

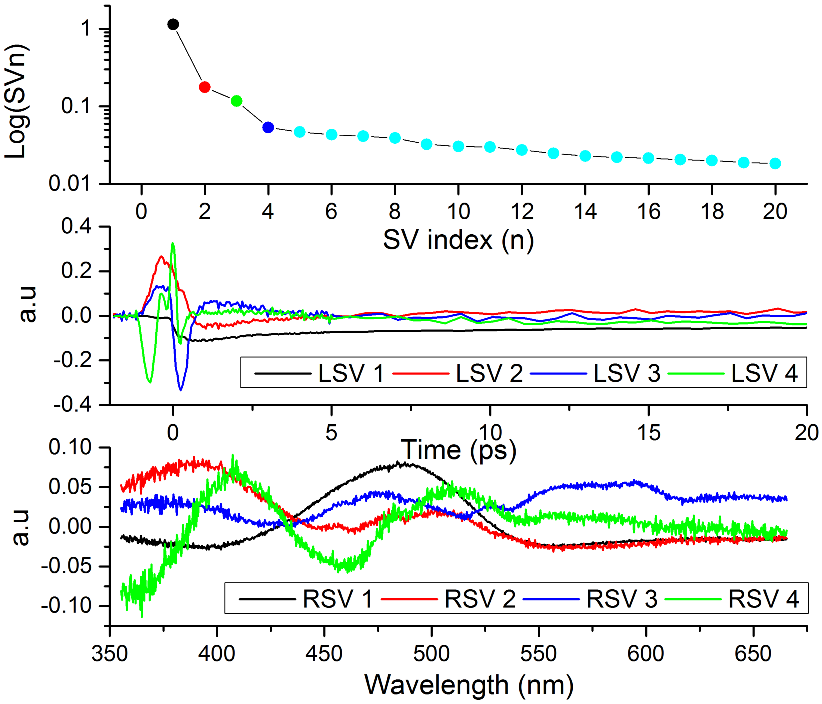

Figure A.5: SVD analysis of the Hg(HDz)$_2$ dataset. Top frame: Singular values. Middle frame: First four left singular values. Bottom frame: First four right singular vectors.

A.4 Pumping the ligand at it's second absorption peak (470 nm)

An in depth analysis of the ligand when pumped at 470 nm was not undertaken due to excitation of both the keto and enol forms of the ligand. The initial global analysis reveals dynamics which are considerably different to those obtained when pumped at 610 nm - i.e the absence of a ≈10 ps component and the presence of a 303 ps component. The difference is highlighted more clearly when the DADS in Figures A.6c and 4.10b are compared. Despite

Stellenbosch University https://scholar.sun.ac.za

the differences we note that the bleaching signal at 610 nm appears instantaneously (see "Bleaching signals" in Section 4.3 for further details).

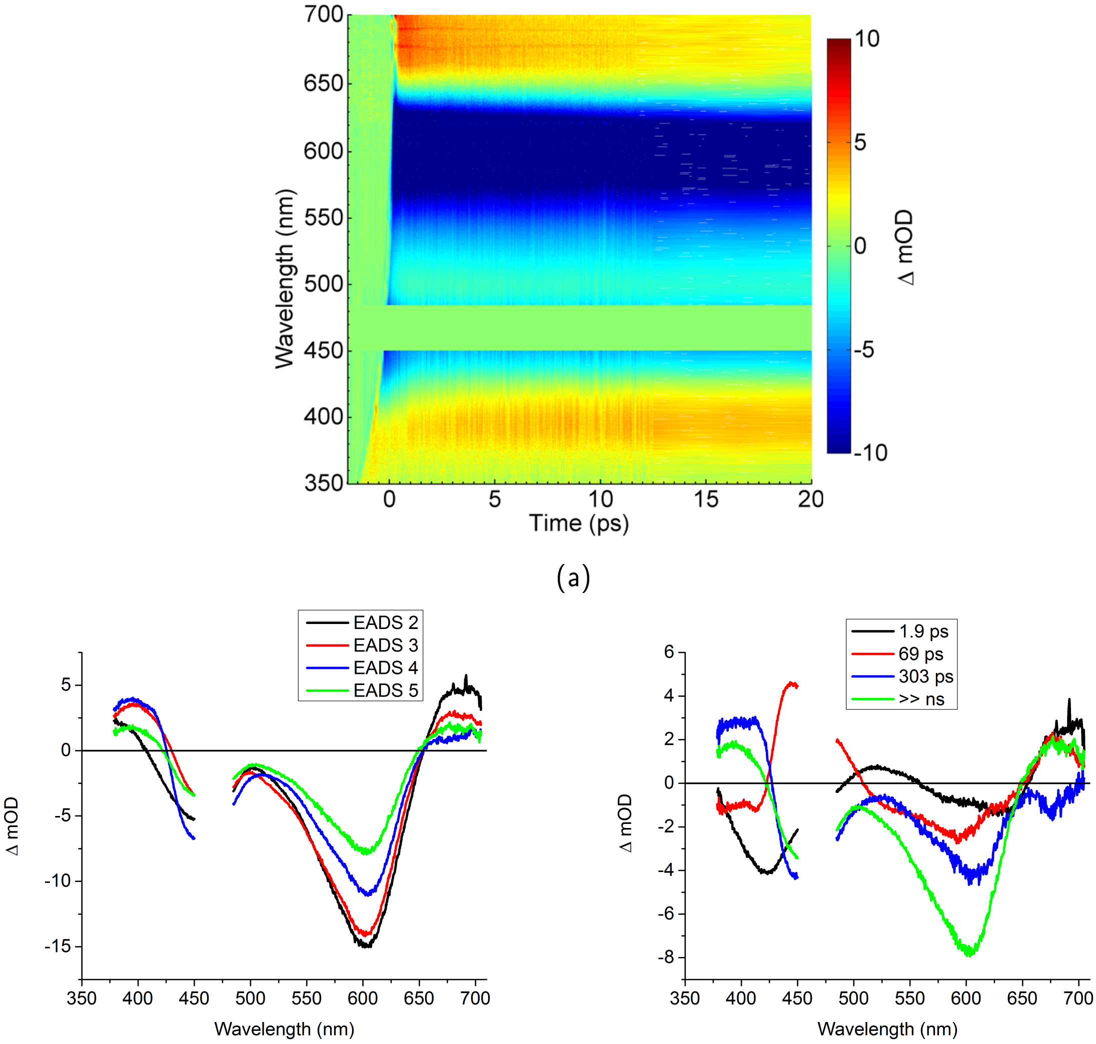

(a)

(b)

(c)

Figure A.6: a) Transient absorption spectrum of the ligand obtained at a pump wavelength of 470 nm. The measurement taken using the CaF_2 supercontinuum spans from 350-650 nm after which a second measurement using the Sapphire-generated supercontinuum has been 'stitched' on from 650-700 nm. b) and c): Respective EADS and DADS resulting from global analysis.

Stellenbosch University https://scholar.sun.ac.za

B Technical aspects

B.1 Transient Measurement Program

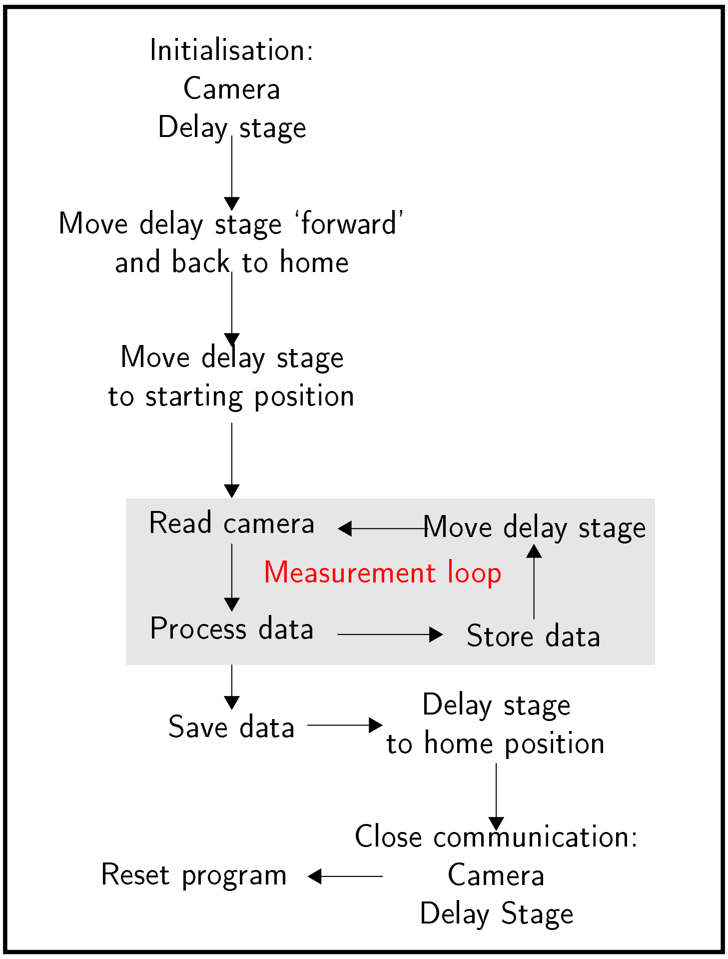

Figure B.1: The TAS measurement program

Figures B.1 and B.2 illustrate the measurement procedure and how components in the laboratory are connected. When the transient absorption measuring program is started, the parameters required for the selected camera (infra-red or visible) and delay stage (10 cm or 30 cm) are set. For example, the delay stage requires parameters such as the motor current, limit switch positions, velocity, acceleration etc. Once the initialisation is complete, the delay stage is moved forward and back to its home position. This ensures that we do not require backlash compensation and that the motor will always start from the same position. Next, the motor is moved to its starting position as specified by the user. The measurement loop now commences.

Stellenbosch University https://scholar.sun.ac.za

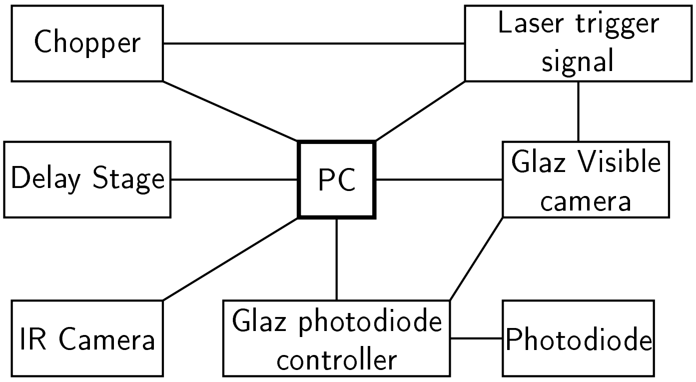

Figure B.2: An overview of how components in the laboratory are connected.

The camera is turned on and captures data until the number of samples specified is reached. Now, depending on whether the IR or Glaz Visible camera is used, the treatment of the data will differ. For the Glaz camera, two separate arrays are collected which contain the averaged pumped and un-pumped spectra - these are separated on the camera depending on the signal that the camera receives from the photodiode. The IR camera operates slightly differently. It passes on an array which contains all the individual spectra as well as the status of the chopper when each spectrum was taken. Consequently, the data first has to be sorted into pumped and unpumped spectra. This data is then averaged and the ratio taken. Following the data processing it is stored in a 'measurement' array which will collect the ratio of the two spectra at different delay stage positions. The delay stage is now moved to its next position and the processes repeats itself. Once the measurement loop is completed, the data in the measurement array is processed according to the measurement range(s) present and written to their respective files. The delay stage is then moved to its home position and communication terminated with the delay stage and camera. The program is then reset in order to make it ready for its next use - this involves resetting the states of various buttons, indicators and variables.

B.2 Technical points: Programs/tasks/modifications

The following list contains contributions that were made during the course of this study to the development and modifications with regards to the experimental setup.

1. Installation of new delay stage controllers.
   Initially a Newport controller was employed for this purpose, however, it was practically significant to replace this controller with a more compact controller. Synertronic Design's Urugan-μ was chosen as this could easily be integrated in LabView. Along with the replacement of the NewPort controller, another longer (30cm) delay stage was also installed with its own Urugan-μ controller. This delay stage would be used in conjunction with a NOPA different to the one used in this study. By having two stages, it was necessary to introduce the ability to choose between the two different stages (and their settings) in all of the existing LabView programs as this functionality was not present.

2. Ocean Optics spectrum capture
   A program used to view and capture the NOPA signal's spectrum. The program was modified using LabView packages supplied with the spectrometer.

Stellenbosch University https://scholar.sun.ac.za

3. White light spectrum capture, optimisation and spectrometer calibration
   This program was already present, but required modifications to incorporate the new cameras.

4. Transient absorption signal optimisation
   The program was altered to accommodate the new cameras as well as the Urugan delay stage controller.

5. Incorporating beam compensation into the existing transient absorption measurement program

6. Modifying the existing TAS program to enable cross-correlated frequency resolved optical gating measurements.

7. Modifications to a pressure monitoring and recording program used by the ultra-fast electron diffraction group.

Stellenbosch University https://scholar.sun.ac.za

B List of References

[1] P Hamm, M Zurek, T R˜sschinger, H Patzelt, D Oesterhelt, and W Zinth. Femtosecond spectroscopy of the photoisomerisation of the protonated Schiff base of all-trans retinal. *Chemical Physics Letters*, 263:613–621, 1996.

[2] Masahiro Irie, Tuyoshi Fukaminato, Takatoshi Sasaki, Naoto Tamai, and Tsuyoshi Kawai. Organic chemistry: a digital fluorescent molecular photoswitch. *Nature*, 420(6917):759–760, 2002.

[3] Karl Deisseroth. Optogenetics. *Nature Methods*, 8(1):26–29, 2011.

[4] Ali Coskun, Michal Banaszak, R. Dean Astumian, J. Fraser Stoddart, and Bartosz a. Grzybowski. Great expectations: can artificial molecular machines deliver on their promise? *Chemical Society Reviews*, 41(1):19, 2012.

[5] Heinz Dürr and Henri Bouas-Laurent. *Photochromism: molecules and systems: molecules and systems*. Gulf Professional Publishing, 2003.

[6] Sameh Helmy, Frank A Leibfarth, Saemi Oh, Justin E Poelma, Craig J Hawker, and Javier Read de Alaniz. Photoswitching using visible light: a new class of organic photochromic molecules. *Journal of the American Chemical Society*, 136(23):8169–72, 2014.

[7] Patrick Feneyrou, Françoise Soyer, Pierre Le Barny, Elena Ishow, Michel Sliwa, and Jacques a Delaire. Photochromic compounds as optical limiters in the nanosecond time range: the example of mercury dithizonate complex. *Photochemical & photobiological sciences : Official journal of the European Photochemistry Association and the European Society for Photobiology*, 2(3):195–202, 2003.

[8] E C Breitner and C L Sloan. Metal Dithizonates. *Journal of the American Chemical Society*, 2118(2):4441–4448, 1961.

[9] Shengwen Qi, Xiuqin Yang, Rui Lu, Kuan Chen, Chunping Zhang, Jianguo Tian, Jingjun Xu, and Qiang Wu. Nonlinear optical properties of mercury dithizonate in a polymer film. *Journal of Modern Optics*, 51(11):1671–1677, July 2004.

[10] Xiuqin Yang, Shengwen Qi, Kuan Chen, Chunping Zhang, Jianguo Tian, and Qiang Wu. Optical limiting characteristics of mercury dithizonate in polymer film. *Optical Materials*, 27(8):1358–1362, May 2005.

[11] Rudi Berera, Rienk van Grondelle, and John T M Kennis. Ultrafast transient absorption spectroscopy: Principles and application to photosynthetic systems, 2009.

[12] Heinrich Schwoerer, Karel G. Von Eschwege, Gurthwin Bosman, Patrizia Krok, and Jeanet Conradie. Ultrafast photochemistry of dithizonatophenylmercury(II). *ChemPhysChem*, 12(14):2653–2658, 2011.

[13] Karel G. Von Eschwege, Gurthwin Bosman, Jeanet Conradie, and Heinrich Schwoerer. Femtosecond laser spectroscopy and DFT studies of photochromic dithizonatomercury complexes. *Journal of Physical Chemistry A*, 118(5):844–855, 2014.

[14] Joris Snellenburg, Sergey Laptenok, Ralf Seger, Katharine Mullen, and Ivo Van Stokkum. Glotaran: a java-based graphical user interface for the r package timp. *Journal of Statistical Software*, 49(3), 2012.

[15] Groupe De Photochimie Organique, Universitiit Saarlandes, C Wentrup, R Guglielmetti, H G Heller, M Irie, J C Micheau, and J L Pozzo. ORGANIC PHOTOCHROMISM Organic photochromism (IUPAC Technical Report). 73(4):639–665, 2001.

Stellenbosch University https://scholar.sun.ac.za

[16] Karel G. Von Eschwege, Jeanet Conradie, and Annemarie Kuhn. Dithizone and its oxidation products: A DFT, spectroscopic, and X-ray structural study. *Journal of Physical Chemistry A*, 115(51):14637–14646, 2011.

[17] P. Jones, P. J. Hobbs, and L. Ebdon. A dithizone post-column detector for the high-performance liquid chromatographic determination of trace metals. *Analytica Chimica Acta*, 149(C):39–46, 1983.

[18] Hossein Tavallali, Gohar Deilamy-Rad, Abolfath Parhami, and Seyede Zahra Mousavi. A novel development of dithizone as a dual-analyte colorimetric chemosensor: Detection and determination of cyanide and cobalt (II) ions in dimethyl sulfoxide/water media with biological applications. *Journal of Photochemistry and Photobiology B: Biology*, 125:121–130, 2013.

[19] U-W Grummt, H Langbein, R Nöske, and G Röbisch. Photochromism and thermochromism of dithizone in solution. *Journal of photochemistry*, 27(2):249–257, 1984.

[20] M.A. Rauf, S. Hisaindee, J.P. Graham, and A. Al-Zamly. Effect of various solvents on the absorption spectra of dithizone and DFT calculations. *Journal of Molecular Liquids*, 211:332–337, November 2015.

[21] M Laing and PA Alsop. The structure of primary nickel dithizonate. *Talanta*, pages 242–244, 1970.

[22] Kumar S Henry Freiser Math. Crystal and molecular structure of zinc dithizonate. *Talanta*, (I):435–437, 1961.

[23] Karel G. Von Eschwege, Jeanet Conradie, and Jannie C. Swarts. A DFT perspective on the structures and electronic spectra of the orange and blue isomers of photochromic dithizonatophenylmercury(II). *Journal of Physical Chemistry A*, 112(11):2211–2218, 2008.

[24] L Armelao, G Bandoli, D Barreca, G Bottaro, E Tondello, A Venzo, and A Vittadini. Molecular photochromic systems : a theoretical and experimental investigation on zinc (II) dithizonate. (Ii):246–254, 2007.

[25] Kumar S Math and Henry Freiser. Some Low-Spin Nickel Chelates with Heterocyclic Nitrogen Bases. 165(6), 1969.

[26] Harry B. Gray and C J Ballhausen. A Molecular Orbital Theory for Square Planar Metal Complexes. *Journal of the American Chemical Society*, 85(3):260–265, 1963.

[27] Vlasta Bonačić-Koutecký and Josef Michl. Photochemical syn-anti isomerization of a Schiff base: A two-dimensional description of a conical intersection in formaldimine. *Theoretica Chimica Acta*, 68(1):45–55, 1985.

[28] Chenwei Jiang, Ruihua Xie, Fuli Li, and Roland E. Allen. Trans-to-cis isomerization of stilbene following an ultrafast laser pulse. *Chemical Physics Letters*, 474(4-6):263–267, 2009.

[29] M. Klessinger and J. Michl. *Excited States and Photo-Chemistry of Organic Molecules*. Wiley, 1995.

[30] William G Herkstroeter. The Mechanism of Syn-Anti Isomerization of Azomethine Dyes. *Journal of the American Chemical Society*, 95(26):8686–8691, 1973.

[31] N. Sertova, I. Petkov, and J.-M. Nunzi. Photochromism of mercury(II) dithizonate in solution. *Journal of Photochemistry and Photobiology A: Chemistry*, 134(3):163–168, 2000.

[32] Alan T Hutton and Harry M N H Irving. Photochromism in Organomercury(II) Dithizonates. 1982.

Stellenbosch University https://scholar.sun.ac.za

[33] Natalie L Cromhout and Alan T Hutton. Photochromic long-chain organomercury (ii) dithizonate complexes in the biphenyl series. *Journal of Coordination Chemistry*, 52(2):169–183, 2000.

[34] Christine Geoslin, Arthur W. Adamson, and Adolfo R. Gutierrez. Photochemical and kinetic studies of some metal dithizonate complexes. *Inorganica Chimica Acta*, 29(C):279–287, 1978.

[35] Gurthwin Bosman. *Transient Absorption Spectroscopy Of Metal Complexes : Dithizonatophenylmercury (II) And Derivatives*. PhD thesis, University of Stellenbosch, 2011.

[36] K. Ekvall, P. van der Meulen, C. Dhollande, L.-E. Berg, S. Pommeret, R. Naskrecki, and J.-C. Mialocq. Cross phase modulation artifact in liquid phase transient absorption spectroscopy. *Journal of Applied Physics*, 87(5):2340–2352, 2000.

[37] A. Brodeur and S. L. Chin. Ultrafast white-light continuum generation and self-focusing in transparent condensed media. *Journal of the Optical Society of America B*, 16(4):637, 1999.

[38] V.P. Kandidov, O.G. Kosareva, I.S. Golubtsov, W. Liu, A. Becker, N. Akozbek, C.M. Bowden, and S.L. Chin. Self-transformation of a powerful femtosecond laser pulse into a white-light laser pulse in bulk optical media (or supercontinuum generation). *Applied Physics B: Lasers and Optics*, 77(2-3):149–165, sep 2003.

[39] Douglass Schumacher. Controlling continuum generation. *Optics letters*, 27(6):451–453, 2002.

[40] Robert W. Boyd. *Nonlinear Optics, Third Edition*. Academic Press, 3rd edition, 2008.

[41] A Brodeur and S L Chin. Band-gap dependence of the ultrafast white-light continuum. *Physical Review Letters*, 80(20):4406–4409, 1998.

[42] E Riedle, M Beutter, S Lochbrunner, J Piel, S Schenkl, S Spörlein, and W Zinth. Generation of 10 to 50 fs pulses tunable through all of the visible and the NIR. *Applied Physics B*, 71(3):457–465, 2000.

[43] I. H M Van Stokkum, Delmar S. Larsen, and Rienk Van Grondelle. Global and target analysis of time-resolved spectra, 2004.

[44] K C Toh, Emina a Stojković, Ivo H M van Stokkum, Keith Moffat, and John T M Kennis. Fluorescence quantum yield and photochemistry of bacteriophytochrome constructs. *Physical chemistry chemical physics : PCCP*, 2011.